JOURNAL OF GEOPHYSICAL RESEARCH, VOL. 105, NO. D10, PAGES 12,123–12,147, MAY 27, 2000

Global distribution of carbon monoxide

Tracey Holloway

Atmospheric and Oceanic Sciences Program, Princeton University, Princeton, New Jersey

Hiram Levy II

Geophysical Fluid Dynamics Laboratory, Princeton, New Jersey

Prasad Kasibhatla

Nicholas School of the Environment, Duke University, Durham, North Carolina

Abstract. This study explores the evolution and distribution of carbon monoxide (CO) using the National Oceanic and Atmospheric Administration (NOAA) Geophysical Fluid Dynamics Laboratory three-dimensional global chemical transport model (GFDL GCTM). The work aims to gain an improved understanding of the global carbon monoxide budget, specifically focusing on the contribution of each of the four source terms to the seasonal variability of CO. The sum of all CO sources in the model is 2.5 Pg CO/yr (1 Pg = 10^3 Tg), including fossil fuel use (300 Tg CO /yr), biomass burning (748 Tg CO/yr), oxidation of biogenic hydrocarbons (683 Tg CO/yr), and methane oxidation (760 Tg CO/yr). The main sink for CO is destruction by the hydroxyl radical, and we assume a hydroxyl distribution based on three-dimensional monthly varying fields given by *Spivakovsky et al.* [1990], but we increase this field by 15% uniformly to agree with a methyl chloroform lifetime of 4.8 years [*Prinn et al.*, 1995]. Our simulation produces a carbon monoxide field that agrees well with available measurements from the NOAA/Climate Monitoring and Diagnostics Laboratory global cooperative flask sampling network and from the Jungfraujoch observing station of the Swiss Federal Laboratories for Materials Testing and Research (EMPA) (93% of seasonal-average data points agree within ±25%) and flight data from measurement campaigns of the NASA Global Tropospheric Experiment (79% of regional-average data points agree within ±25%). For all 34 ground-based measurement sites we have calculated the percentage contribution of each CO source term to the total model-simulated distribution and examined how these contributions vary seasonally due to transport, changes in OH concentration, and seasonality of emission sources. CO from all four sources contributes to the total magnitude of CO in all regions. Seasonality, however, is usually governed by the transport and destruction by OH of CO emitted by fossil fuel and/or biomass burning. The sensitivity to the hydroxyl field varies spatially, with a 30% increase in OH yielding decreases in CO ranging from 4-23%, with lower sensitivities near emission regions where advection acts as a strong local sink. The lifetime of CO varies from 10 days over summer continental regions to well over a year at the winter poles, where we define lifetime as the turnover time in the troposphere due to reaction with OH.

1. Introduction

The global distribution of carbon monoxide (CO) holds interest from several perspectives: as a primary and secondary determinant of air quality, as the leading sink of hydroxyl (OH) radicals, and as an atmospheric tracer with a relatively long lifetime, that is, an indicator of how transport redistributes pollutants on a global scale.

As a determinant of air quality, high CO concentrations can directly affect human health, and indirectly CO plays a role in catalytic ozone production and destruction. The direct effects of CO only occur at high concentrations not observed on regional scales (e.g., 100 ppm [*Seinfeld*, 1986]). Thus, for the present global investigation, CO has the greatest air quality impact, given sufficient NO_x, as a precursor to tropospheric ozone, a secondary pollutant associated with respiratory problems and decreased crop yields [e.g., *McKee*, 1993; *Chameides et al.*, 1994]. A quantification of the CO distribution is needed for an accurate estimate of O_3 chemistry.

The importance of CO in ozone chemistry may be better understood by looking at the catalytic destruction and production cycles in which CO plays a part. This chemistry is not included in the current CO simulation, but is presented here to illustrate the role of carbon monoxide in the ozone budget. For a discussion of ozone simulations with CO fields similar

Paper number 1999JD901173.
0148-0227/00/1999JD901173$09.00

to those discussed here, see *Klonecki and Levy* [1997], *Klonecki* [1999], and *Levy et al.* [1997].

Initial ozone destruction creates hydroxyl radicals:

(R1) $O_3 + h\nu \rightarrow O^1D + O_2$ (<315 nm)

(R2) $O^1D + H_2O \rightarrow 2OH$

The one photochemical sink for CO is reaction with the OH radical (reaction (R3), below). Depending on available NO_x, this oxidation may produce or destroy ozone. The threshold separating the "high NO_x" case from the "clean" case is ~100 parts per trillion by volume (pptv) NO_x at 990 mbar and ~30 pptv NO_x at 500 mbar [*Klonecki*, 1999].

If high NO_x is present, ozone production is as follows:

(R3) $CO + OH \rightarrow H + CO_2$

(R4) $H + O_2 + M \rightarrow HO_2 + M$

(R5) $HO_2 + NO \rightarrow NO_2 + OH$

(R6) $NO_2 + h\nu \rightarrow NO + O$ (<425 nm)

(R7) $O + O_2 + M \rightarrow O_3 + M$

$CO + 2O_2 \rightarrow O_3 + CO_2$

If clean, continued ozone destruction is as follows:

(R3) $CO + OH \rightarrow H + CO_2$

(R4) $H + O_2 + M \rightarrow HO_2 + M$

(R8) $HO_2 + O_3 \rightarrow OH + 2O_2$

(R9) $CO + OH \rightarrow CO_2 + H$

(R10) $H + O_2 + M \rightarrow HO_2 + M$

$2CO + O_3 + OH \rightarrow 2CO_2 + HO_2$

In the presence of high NO concentrations the HO_2 product of CO destruction loses an oxygen atom to form NO_2, which rapidly dissociates to form ozone. In the absence of NO_x, the HO_2 molecule reacts directly to destroy O_3.

Aside from its role in ozone chemistry, CO is an interesting compound to investigate. As an atmospheric tracer with a moderately long lifetime and relatively simple chemistry, CO illuminates the role of transport in redistributing chemical pollutants. An analysis of the spatial and seasonal variability of CO permits insight into the relative influence of source regions, transport, and chemical destruction on the global distribution.

The current investigation uses the global chemical transport model from the National Oceanic and Atmospheric Administration (NOAA) Geophysical Fluid Dynamics Laboratory (GFDL GCTM) to simulate the CO distribution. The GCTM uses model-generated winds for one representative year to advect the CO emitted from fossil fuel burning, biomass burning, oxidation of biogenic hydrocarbons, and methane oxidation. We describe the model's meteorology as that of a "representative year" because it does not simulate any one particular year, but exhibits values and variability characteristic of the real atmosphere.

Other efforts to model the global CO distribution with a three-dimensional (3-D) chemical transport model (CTM) include *Pinto et al.* [1983], the first study of the global CO budget with a 3-D model (8°x10° horizontal resolution, seven vertical levels, general circulation model (GCM) winds); *Saylor and Peters* [1991] running the GLOBAL model (5°x5° horizontal resolution, nine vertical levels, analyzed winds for 1 month); *Muller and Brasseur* [1995], using the IMAGES model (5°x5° horizontal resolution, 25 vertical levels, monthly mean analyzed winds); *Allen et al.* [1996], examining interannual variability with the Goddard CTM (2°x2.5° horizontal resolution, 20 vertical levels, analyzed winds); *Berntsen and Isakson* [1997], running the NASA Goddard Institute for Space Studies (GISS) CTM (8°x10° horizontal resolution, nine vertical levels, GCM winds); *Brasseur et al.* [1998] and *Hauglustaine et al.* [1998], simulating multiple species with the National Center for Atmospheric Research (NCAR) Measurement of Ozone and Water Vapor by Airbus In-Service Aircraft (MOZART) model (2.8°x2.8°, 25 vertical levels, GCM winds); and *Wang et al.* [1998] running the Harvard CTM (4°x5° horizontal resolution, seven vertical levels, GCM winds). Details on CO emissions and OH fields used in the more recent studies are outlined in Table 1. For a specific discussion of CO variations between global chemical transport models, the reader is directed to *Kanakidou et al.* [1999]. That paper presents results from the Global Integration Modelling/International Global Atmospheric Chemistry Project (GIM/IGAC) 1997 intercomparison exercise. Because our simulations were not complete in 1997, these results from the GFDL GCTM are not included in the Kanakidou et al. paper.

This work presents a detailed study of the global carbon monoxide budget using a GCTM focusing on the role of each of the assumed four CO sources in controlling the spatial and seasonal variability of carbon monoxide, an issue which has not been dealt with in such detail previously. We also present the most extensive comparison results from a single model with measurements yet published. The analysis presented here of model results compared with observations lends insight into the global CO cycle, the composition of observed CO seasonality, and our understanding of the CO emission fields which were used in these simulations.

2. The Model

The current study uses the NOAA Geophysical Fluid Dynamics Laboratory Global Chemical Transport Model (GFDL GCTM). The horizontal resolution is approximately uniform at ~270 km x 270 km (zonal resolution of 2.4° and meridional resolution of 2.4° at the tropics; 5.7° at 65° N/S) and 11 vertical levels (centered at 10, 38, 65, 110, 190, 315, 500, 685, 835, 940, 990 mbar). Past studies have employed the GCTM to simulate NO_x [*Levy et al.*, 1999], ozone [e.g., *Yienger et al.*, 1999; *Levy et al.*, 1997; *Kasibhatla et al.*, 1996], and sulfur [*Kasibhatla et al.*, 1997]. The model is run separately for each species it simulates, so the CO experiments presented here were run with only methane oxidation and CO destruction by hydroxyl reactions included. By separating out the chemistry of each family of compounds, the GCTM is uniquely well-suited for the type of detailed budget analysis discussed here.

Off-line 6-hour averaged winds from an earlier GFDL general circulation model (GCM) drive advection for one repre-

Table 1. CO Sources Compared With Other Recent Studies

	GFDL GCTM	*Wang et al.* [1998]	*Brasseur et al.* [1998]; *Hauglustaine et al.* [1998]	*Berntsen and Isaksen* [1997]	*Allen et al.* [1996]	*IPCC* [1992]	EDGAR *(Olivier et al.* [1994])	*Kanakidou* et al. [1999]
Fossil fuel	300	390	381.6	650	329	130	297	303-893
Biomass burning (includes wood fuel)	748	650	661.8	800	370	310	677	450-920
Biogenic HC oxidation	683	290	see below	NA	618	NA	NA	see below
Methane oxidation	760	800 (includes NMHC oxidation)	881	NA	722	NA	NA	840-1459
Oceans	---	---	13	50	---	17	NA	0-378
Direct biogenic emissions	---	---	162.1	75	---	43	NA	0-387
Total	2491	2130	2100	1575 + ?	2039	499 + ?	974 + ?	1218-2742
CH_3CCl_3 lifetime, years	4.8*	5.1†	NA†	4.3†	5.5*	---	---	---

NA, not applicable
*Denotes a study with fixed OH fields. †Denotes a study with OH fields calculated on-line.

sentative (climatological realistic) model year (see *Mahlman and Moxim* [1978] and the appendix of *Levy et al.* [1999] for details of the GCTM's transport module; see *Manabe et al.* [1975] and *Manabe and Holloway* [1974] for details of parent GCM). The benefits of such a global model include self-consistent three-dimensional wind, temperature, and precipitation fields, as well as self-consistent subgrid-scale processes. This "self-consistency" means that meteorological variables work together to satisfy the equations describing the thermodynamics and fluid dynamics of the atmosphere, a condition difficult to guarantee with interpolated or assimilated data.

The model does not include any interannual variability, nor does it have diurnal insolation. Initializing the model with a previous simulation of tropospheric carbon monoxide, the system is run to a steady state seasonal cycle. After 2 years, the model has less than 1% deviation from this steady state cycle for levels below 110 mbar in the midlatitudes and tropics (less than 5% deviation at poles). This simulation of CO evolved from an earlier study by *Kasibhatla et al.* [1996].

3. Sources and Sinks

The sum of all CO sources in the model is 2491 Tg CO/yr, including fossil fuel use, biomass burning, oxidation of biogenic hydrocarbons, and methane oxidation. Table 1 shows a comparison of global emissions used in the present investigation with those in previous studies, and with CO emission estimates from the Intergovernmental Panel on Climate Change (IPCC) IS92a scenario [*IPCC*, 1992], the Emission Database for Global Atmospheric Research (EDGAR) [*Olivier et al.*, 1994], and the range of emissions given by *Kanakidou et al.* [1999].

The assumed fossil fuel emissions add up to a total of 300 Tg CO/yr, with 282 Tg CO/yr emitted in the Northern Hemisphere and 18 Tg CO/yr emitted in the Southern Hemisphere (Figure 1a). The emissions estimate employed is based on the two-level, seasonal scenario for anthropogenic NO_x emission from the Global Emissions Inventory Activity (GEIA), part of the International Global Atmospheric Chemistry Program (IGAC) [*Benkovitz et al.*, 1996]. The 1985 GEIA estimate was extrapolated to 1990 levels using energy data from the *U.S. Energy Information Administration* (EIA) [1997]; (J. Yienger, personal communication, 1998), with the substitution of 1990 emissions in Asia from *van Aardenne et al.* [1999]. This NO_x inventory was converted to CO using a CO:NO_x ratio of 6.7, derived from 1990 U.S. Environmental Protection Agency (EPA) emission data [*EPA*, 1997]. Our approach of scaling the NO_x fossil fuel emissions to estimate CO is reasonable because the combustion processes which emit NO_x are generally responsible for CO emissions as well. An alternate approach would be to use an emissions estimate developed specifically for CO from fossil fuel combustion, such as the EDGAR database [*Olivier et al.*, 1994]. As noted in Table 1, however, the global total fossil fuel CO emission estimate from the EDGAR study (297 Tg CO/yr) is very similar to our estimate of 300 Tg CO/yr.

The GEIA global NO_x scenario incorporates country-by-country fossil fuel use statistics allocated to a 1°x1° grid based on population, and updates this estimate with best available regional emission calculations. Uncertainties associated with our use of this source to calculate CO arise from uncer-

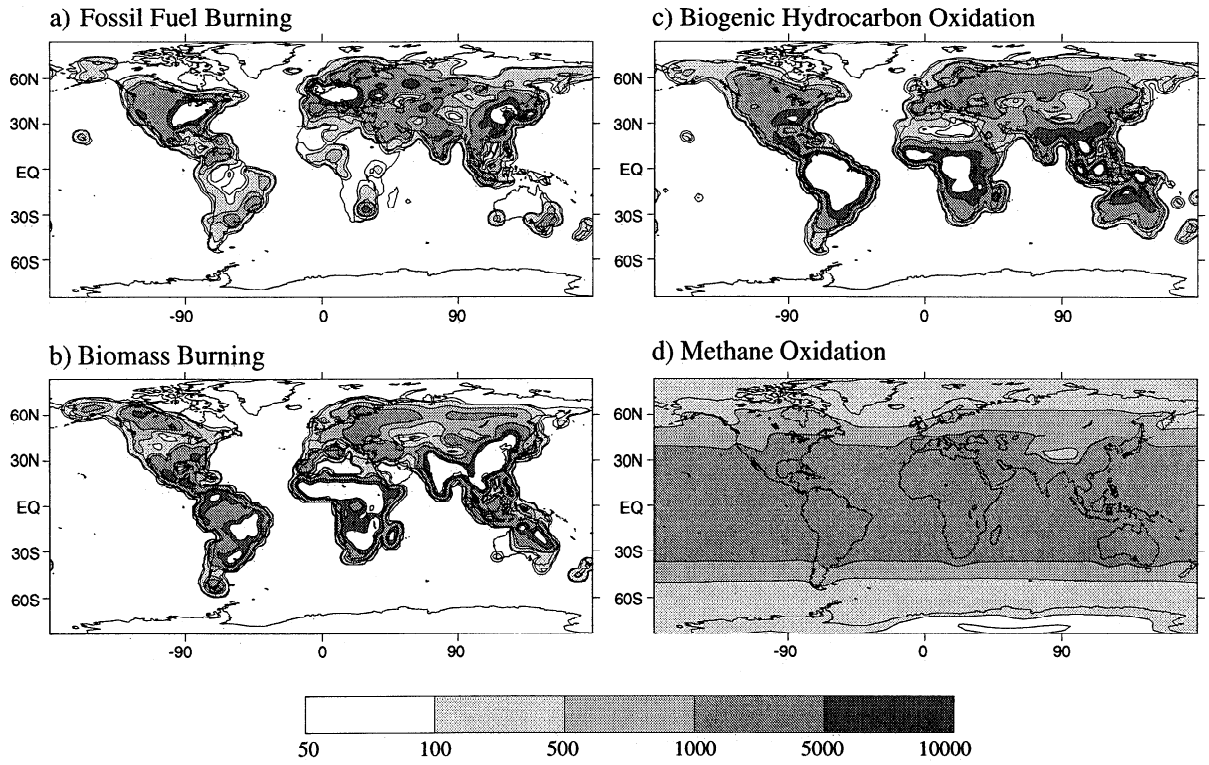

Figure 1. CO emissions sources in GCTM in kg km^{-2} yr^{-1} (white within black denotes values greater than 10,000 kg km^{-2} yr^{-1}). (a) Annual fossil fuel emissions. (b) Annual biomass burning emissions. (c) Annual input of CO from biogenic hydrocarbon oxidation. (d) Annual input of CO from methane oxidation.

tainties in the GEIA NO_x inventory (which have been classified regionally as "high," "medium," or "low" uncertainty), from the extrapolation of this source to 1990 levels, and from the applicability of the uniform U.S. EPA CO:NO_x scaling factor. The estimate of 1985 NO_x emissions from North America, Europe, Australia, and South Africa are rated as having "low uncertainty;" emissions from Asia as having "medium uncertainty;" and the rest of the world as having "high uncertainty" [*Benkovitz et al.*, 1996]. Most fossil fuel emissions come from North America, Europe, and Asia, regions of higher certainty estimates. No uncertainty estimates are available for EIA global energy consumption statistics used for extrapolation, though data from Organization for Economic Co-operation and Development (OECD) countries are generally considered most reliable. Our assumption of a uniform CO to NO_x conversion factor introduces additional uncertainty. We apply the U.S. EPA 1990 CO to NO_x ratio to all global fossil fuel emission regions, which is probably too low for some countries and too high for others. In the United States this ratio has dropped steadily since 1980 (1980 U.S. ratio: 7.7 [*EPA*, 1997]) because CO emissions have declined more rapidly than NO_x emissions. The drop in CO emissions from fossil fuel burning is attributed to emission controls in new vehicles since transportation accounts for about 80% of anthropogenic U.S. CO emissions [*EPA*, 1997]. The same level of CO reduction would not be expected worldwide. Nonetheless, both China and Europe have CO:NO_x ratios lower than the United States. For example, the CO:NO_x scaling factor for fossil fuels in China is about 5.8 (D. Streets, personal communication, 1999). This reflects higher NO_x emissions relative to CO, and the different sectoral makeup of the emission field. In Europe the emission factor is slightly lower than that in the United States: for all 27 European countries the 1990 emission factor is 6.3 (CORINAIR 90 emissions data, European Topic Centre on Air Emissions, available at http://www.aeat.co.uk/netcen/corinair/corinair.html, 1990).

As seen from a comparison of our fossil fuel emissions with those of other recent studies, our estimate of global total fossil fuel emissions is at the lower end of other recent estimates. As we compare our results with observations in the following discussion, we will consider the question of whether our fossil fuel source is, in fact, unrealistically low.

Our biomass burning source contributes 748 Tg CO/yr (498 Tg CO/yr in the Northern Hemisphere, 250 Tg CO/yr in the Southern Hemisphere), which includes burning of savanna, forests, agricultural residue, fuelwood, and animal waste [*Galanter et al.*, 2000] (Figure 1b). The source combines best available estimates of global partitioning between component burning types (forest, savanna, fuelwood, crop residues, and animal waste) (in the tropics [*Hao and Liu*, 1994]; elsewhere all biomass burning is assumed to be forest); timing [*Richardson*, 1994; *Olson et al.*, 1999, and references therein; *Galanter et al.*, 2000]; and regional biofuel use in Asia [*Streets and Waldhoff*, 1998] with an original global biomass burning estimate [*Levy et al.*, 1991, and references therein; J. A. Logan, private communication, 1990] which has been used in previous studies with the GFDL GCTM. Emissions from biomass burning are concentrated in tropical and subtropical forests and grasslands, with timing of input into the model based on regional climatology, cultural practices, and

satellite observations [*Galanter et al.*, 2000, and references therein]. For example, southern Africa burns from June through November; the northern Sudan/Sahel region burns from October through January; the Amazon Basin of South America burns from June through August; and Southeast Asia burns biomass from January through May, but uses biofuels year round (Figures 5a and 5c show major burning regions in January and July as those areas with a large fraction of CO from biomass burning at 990 mbar). Previous estimates of global biomass burning ranged from 300 to 1600 Tg CO/yr [*Warnek*, 1988, and references therein; *Andreae*, 1991; *Crutzen and Andreae*, 1990], but we see in Table 1 that most recent studies have estimated CO from biomass burning to be 650-800 Tg CO/yr. Thus our estimate is on the high end of previous estimates, but within an increasingly narrowly defined range.

The oxidation of biogenic hydrocarbons supplies a total of 683 Tg CO/yr (342 Tg CO/yr in the Northern Hemisphere, 341 Tg CO/yr in the Southern Hemisphere, see Figure 1c) reflecting the monthly varying emissions of isoprene, monoterpene, and other volatile organic compounds. These hydrocarbons are assumed to be immediately oxidized, yielding 2.76 molecules CO per molecule of oxidized hydrocarbon. The biogenic hydrocarbon emissions are taken from the GEIA estimates [*Guenther et al.*, 1995] with the CO yield from *Miyoshi et al.* [1994] for high-NO_x conditions. The GEIA estimate only includes emissions from the oceans and from plant foliage, which most likely contribute over 95% to the total natural nonmethane hydrocarbon (NMHC) emissions (Figures 6a and 6c show major biogenic emission regions in January and July as those areas with a large fraction of CO from biogenic hydrocarbon oxidation at 990 mbar). The uncertainty associated with this source is estimated to be at least a factor of 3 [*Guenther et al.*, 1995]. The use of the oxidation yield rate contributes additional uncertainty. Although *Miyoshi et al.* [1994] give the high-NO_x rate as an upper bound, it applies only to isoprene. As the Guenther et al. emission estimate reflects a wide range of hydrocarbons, the yield rate for isoprene would be expected to be lower than for larger hydrocarbons. Thus errors from the choice of yield rate act in opposite directions, possibly leading to some cancellation in error terms. As shown in Table 1, our emissions of CO from biogenic hydrocarbon oxidation are higher than recent studies.

Methane (CH_4) oxidation serves as the only CO source with input at all levels of the atmosphere, totaling 760 Tg CO/yr in our model (413 Tg CO/yr in the Northern Hemisphere, 347 Tg CO/yr in the Southern Hemisphere, see Figure 1d). The reaction of methane with the hydroxyl radical yields CO as a product. Thus this CO source depends on the distributions of OH and methane. Methane is taken to be well-mixed in each hemisphere, with 1990 values of 1.78 ppm in the Northern Hemisphere and 1.64 ppm in the Southern Hemisphere [*Dlugokencky et al.*, 1994]. Uncertainty in this source arises primarily from the 100% CO yield assumed for the methane oxidation chain. *Tie et al.* [1992] find that the average annual yield of CO from methane oxidation is 82%, so our methane source may be too large. Uncertainty in the methane oxidation source may also be due to the OH field, discussed below. The total production of CO from methane oxidation falls well within estimates from previous studies (Table 1).

We assume that the one sink for CO in the model is oxidation by OH (reaction (R3) above) which balances the sum of sources at 2491 Tg CO/yr. In addition, the hydroxyl field helps determine the CO produced from methane oxidation. Our OH fields are monthly varying and three-dimensional, taken as 15% higher than *Spivakovsky et al.* [1990]. Our base case was chosen to agree with the 4.8 year lifetime for methyl chloroform (CH_3CCl_3) from *Prinn et al.* [1995]. The original *Spivakovsky et al.* [1990] OH estimates produce a 5.5 year lifetime for CH_3CCl_3. Assuming that average OH concentration is inversely proportional to average lifetime of CH_3CCl_3, a scaling factor of 1.15 was uniformly applied to the *Spivakovsky et al.* [1990] OH concentrations globally. Current global tropospheric mean OH values calculated by C. Spivakovsky (personal communication, 1999) are 33% higher than their 1990 estimate, though the fraction of OH below 700 mbar has decreased from 42% in the 1990 study to 33% in the newer estimate. The total column increase is due to changes in reaction rates and in the distributions of OH precursors, while the decrease in the fraction of OH in the lower troposphere results primarily from the inclusion of nonmethane hydrocarbons in the new simulation (no hydrocarbons were included in the work of *Spivakovsky et al.* [1990] and from higher reflectivity of clouds in the tropics. This suggests that their revised OH fields are higher in the upper troposphere and lower in the lower troposphere than the base case in this study. It is worth noting, however, that their 33% total column OH increase, combined with the 21% decrease in the fraction of OH below 700 mbar leads to an increase of 11% in OH below 700 mbar, only 4% less than our scaling of the *Spivakovsky et al.* [1990] estimate. Table 1 indicates the methyl chloroform lifetime corresponding with OH fields used in each study.

An important issue pertaining to our implementation of OH is justification for our use of prespecified fields. The advantage of specified OH fields is that they provide an estimate of the hydroxyl distribution which is independently constrained by the methyl chloroform lifetime. Since we wish in this study to employ an accurate OH field, not necessarily to calculate an OH field, using a prespecified OH field is a reasonable and computationally efficient solution. There are, however, two questions which must be considered: Does the lack of short-term feedbacks between CO and OH affect the result? Does the lack of longer-term feedbacks between CO and OH affect the results? In answer to the issue of short-term feedbacks, we assert that daily variations in a short-lived species such as OH do not significantly effect the concentrations of CO, which, with lifetimes of the order of 2 weeks to a few months, are influenced by OH changes on larger spatial and temporal scales. While the lack of feedbacks on the monthly and larger timescales may have more of an influence, the *Spivakovsky et al.* [1990] OH was calculated with CO fields based on CO observations, and, as will be discussed (see "Sensitivity Analysis"), CO in the lower troposphere continental regions exhibits low sensitivity to changes in the monthly OH fields.

The OH distribution determines the lifetime of CO, shown in Figures 2a-2d. Over continents in the summer, lifetimes can drop to 10 days, whereas over the winter pole the lifetime of CO is well over a year. Hydroxyl concentrations depend on incoming solar radiation, as well as chemical precursors including ozone and NO_x. The summer continents have the highest OH (shortest CO lifetime) because the summer hemisphere receives greater amounts of solar radiation and because the continental regions have a higher albedo, higher NO_x, and higher O_3 concentrations than do marine areas. Lifetime in-

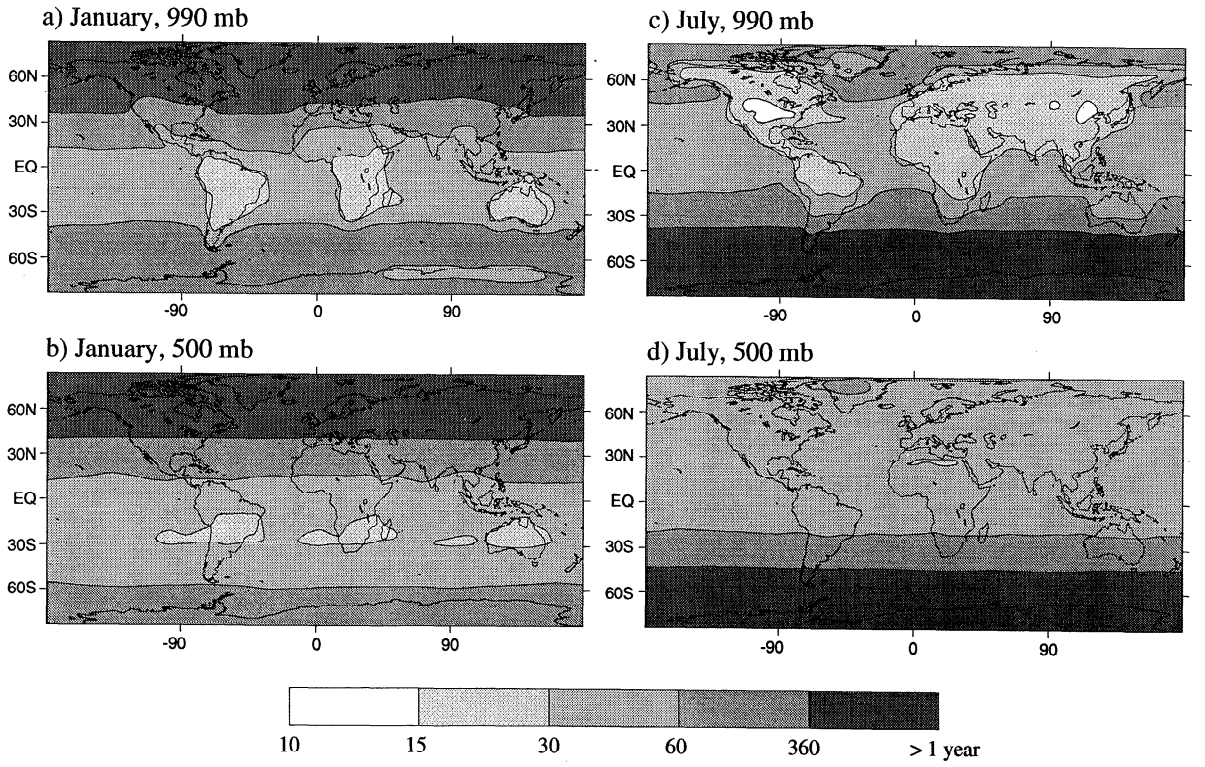

Figure 2. CO lifetime in days. (a) January, 990 mbar. (b) January, 500 mbar. (c) July, 990 mbar. (d) July, 500 mbar.

creases at higher altitudes and in the winter hemisphere. *Spivakovsky et al.* [1990] estimate that about half of the continental enhancement is due to albedo effects, with the other half due to increased hydroxyl precursor concentrations. However, our continental OH fields may be too high because they do not include the effects of nonmethane hydrocarbons [*Spivakovsky et al.*,1990].

Possible sources omitted from the model include direct emission of CO from the ocean, land plants, and soils, as well as oxidation of hydrocarbons released from fossil fuel and biomass burning. On the basis of previous estimates the sum of these sources might contribute up to 2-15% [*Warneck*, 1988, and references therein; *Bates et al.*, 1995, and references therein]. A possible sink omitted from the model is the uptake of CO by soil microorganisms., which has been estimated to be 115-230 Tg CO/yr [*Sanhueza et al.*, 1998].

As pointed out in the preceding discussion, an overall comparison of our emission fields and OH field has been outlined in Table 1. Overall, we have the greatest amount of total CO emissions of all compared models. We will return to the comparison of our CO simulation with that of previous authors after discussing our results and comparing with available data. The emission fields described above were not adjusted (or "tuned") at all to agree the observed CO data discussed here.

4. Results

The model was run to investigate five cases: the CO distribution from all sources and the distribution resulting from each of the four sources taken individually. To minimize numerical nonlinearities arising from the model's advection scheme, the simulations for individual sources were performed by running the model without one source, then subtracting the result from the full source simulation. This approach produces more accurate results because it avoids unrealistically steep concentration gradients which would arise near emission regions if we were running each source individually.

The monthly average distribution of CO for the sum of four sources is shown at 990 mbar and 500 mbar levels for January and July (Figures 3a-3d). A distinct north-south gradient in the background CO concentration is evident in January, but absent in July. This seasonal difference depends on the seasonal variation of OH concentration compared to the hemispheric difference in emissions. The Northern Hemisphere has greater CO emissions than the Southern Hemisphere yearround. During the Northern Hemisphere winter, OH concentrations are low in the Northern Hemisphere and high in the Southern Hemisphere. Thus CO has a longer lifetime in the Northern Hemisphere, reinforcing the effect of the higher Northern Hemisphere emissions. In the summer, however, the effects balance. The OH sink for CO is greatest in the heavily emitting Northern Hemisphere, balancing the low-sink low-source CO budget of the Southern Hemisphere. The distribution in October (not shown) resembles that in July, with the primary difference being the higher CO concentrations stretching over the Northern Hemisphere above 30°N in both the lower and middle troposphere, and less pronounced CO maxima near Northern Hemisphere emission regions. In April the CO distribution (not shown) retains the steep hemispheric gradient characteristic of the January distribution, but with higher concentrations over Mexico and lower over equatorial Africa, both due to changes in the seasonality of our biomass burning source. It is also noteworthy that even at 10°N over

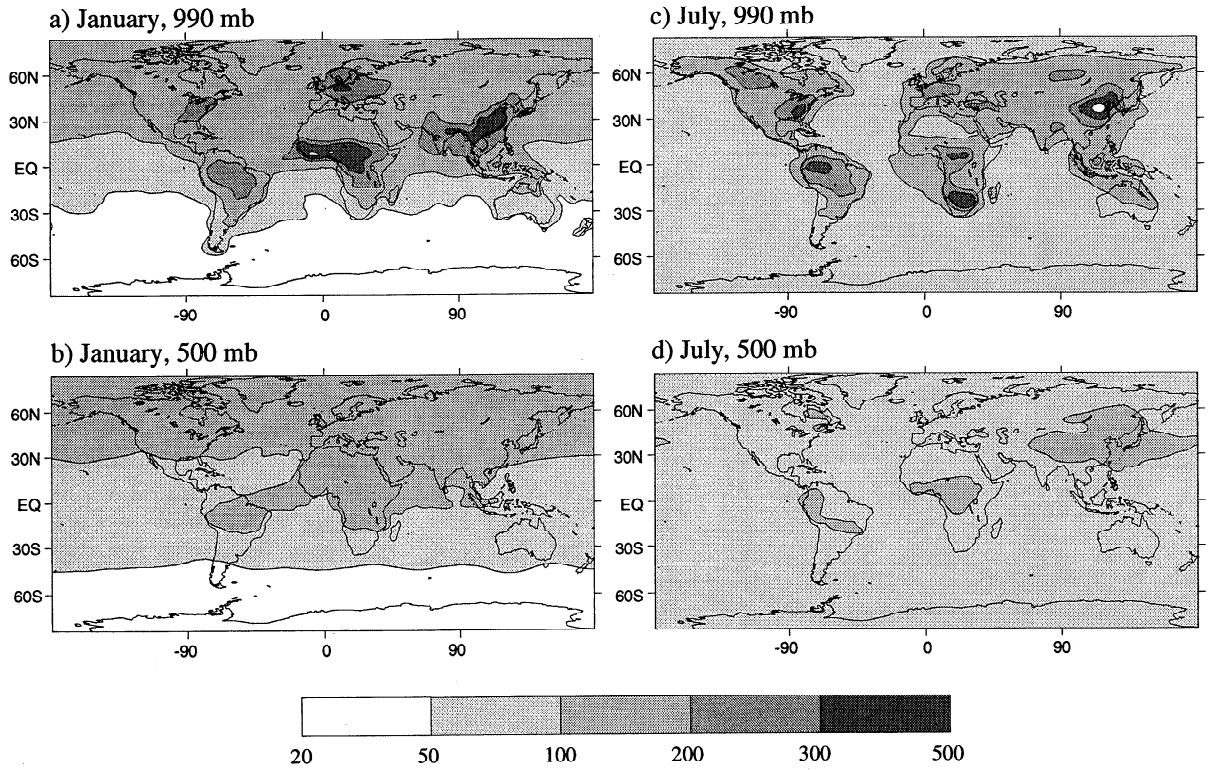

Figure 3. CO distribution in ppb (white within black denotes values greater than 500 ppb). (a) January, 990 mbar. (b) January, 500 mbar. (c) July, 990 mbar. (d) July, 500 mbar.

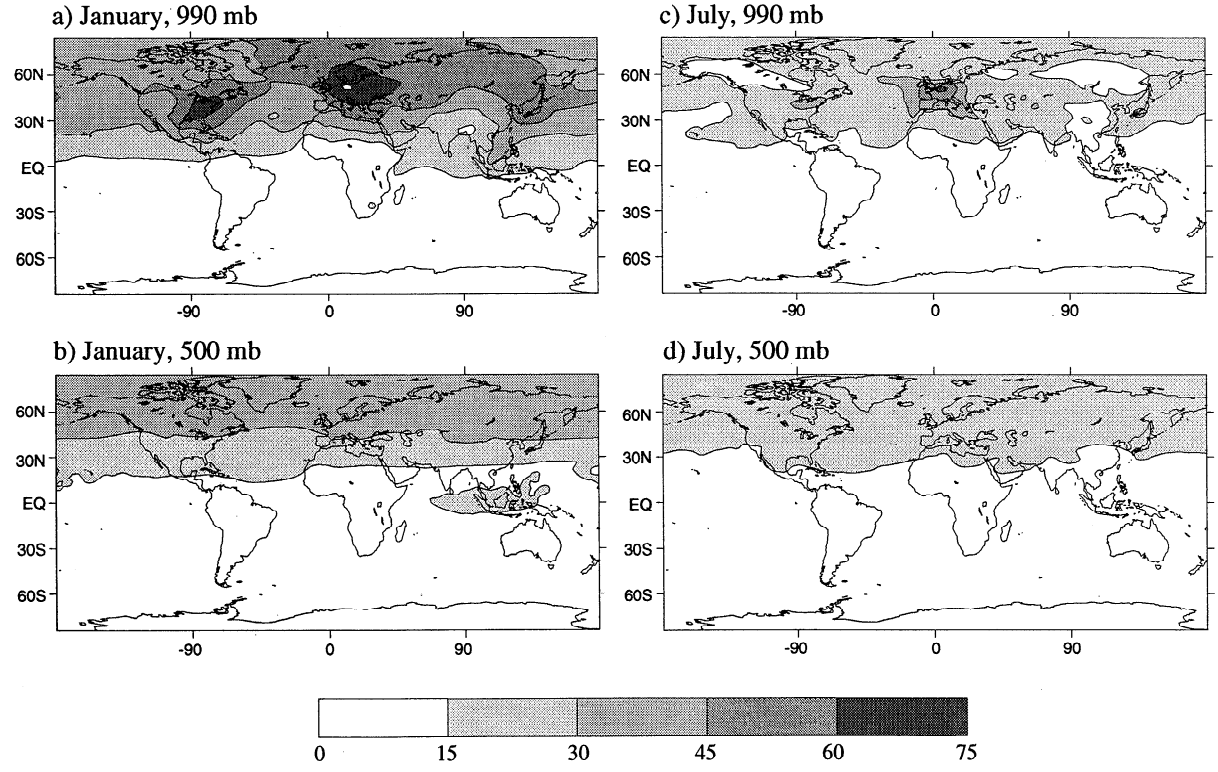

Figure 4. Percentage of total CO distribution from fossil fuel. (a) January, 990 mbar. (b) January, 500 mbar. (c) July, 990 mbar. (d) July, 500 mbar.

the Pacific Ocean, CO concentrations greater than 100 ppb are maintained by the eastward transport of emissions from Asia during this time. During all seasons, highest CO concentrations are found at the surface near emission regions. At the 500 mbar level, higher wind speeds and longer CO lifetimes permit transport over greater distances. Examples include the plume of high CO from Africa spreading over the Atlantic at 500 mbar in January (Figure 3b), as well as that extending eastward from Asia at 500 mbar in July (Figure 3d).

Figures 4a-4d show the percentage CO from fossil fuel. The January meridional gradient observed in the full CO distribution is extremely pronounced for the fossil-only scenario, verifying the intuitive conclusion that the Northern Hemispheric CO concentration bias is largely due to industrialization. At the surface the percentage contribution of fossil fuel averaged over the Northern Hemisphere is 34% in January and 16% in July, but only 5-6% in the Southern Hemisphere. An interesting surface feature of Figure 4a is the large pool of high fossil fuel contribution (>45% of CO) extending westward over Greenland from Europe. A parallel northward extent is not seen around the heavily emitting area of the northeastern United States. The higher latitude of industrialized Europe causes some CO emitted from this region to be caught up in the polar easterlies and carried west over Greenland. The January 500 mbar level shows near zonal homogeneity, reflecting the longer CO lifetimes at higher altitudes, as well as greater mixing in the zonal than meridional direction. During July the surface level distribution lacks the large pools of high fossil fuel CO and the strong north-south gradient seen in January. The shorter lifetime of CO during the summer, as well as greater vertical mixing from a thicker summertime boundary layer, limits transport in both the zonal and meridional directions. As in January, the 500 mbar level in July shows more complete zonal mixing and a smoother north-south gradient, both due to the longer lifetime at this level and greater distance from sources.

The percentage contribution of biomass burning to the global CO distribution is depicted in Figures 5a-5d. Whereas fossil fuel emissions control the large-scale hemispheric CO gradient, biomass burning controls more localized regions near the surface, primarily in the tropics, and contributes 15-30% to CO concentrations throughout most of the troposphere. In January most burning occurs in Africa between the equator and 30°N. These emissions create a strong low-level pool over the equatorial Atlantic. During this time the northern branch of the Hadley circulation is strongest. Emissions in the northern tropics are carried southward at the surface, then lifted and transported northward in the upper troposphere. When this northern Hadley Cell intersects the midlatitude westerlies, high-CO air quickly mixes eastward. Thus the pattern at 500 mbar (Figure 5b) shows a plume of CO from biomass burning extending over the Indian Ocean, combining with biomass burning from Asia, and reaching across the Pacific basin. In July, burning regions in Africa are south of their January locations, whereas burning regions in Asia are farther north. The summer burning in Asia creates a plume stretching over the Pacific between 30°N and 60°N, curling north toward Alaska (Figure 5d).

Figures 6a-6d show that CO over much of South America is controlled by biogenic hydrocarbon oxidation year-round. The gradient of the biogenic CO contribution is steepest in the Northern Hemisphere winter, when there is little vegetative activity in the Northern Hemisphere, and emissions from fossil fuel make up the largest fraction of ambient CO. As with biomass burning from Africa, the impact of CO coming from biogenic hydrocarbon oxidation in South America moves

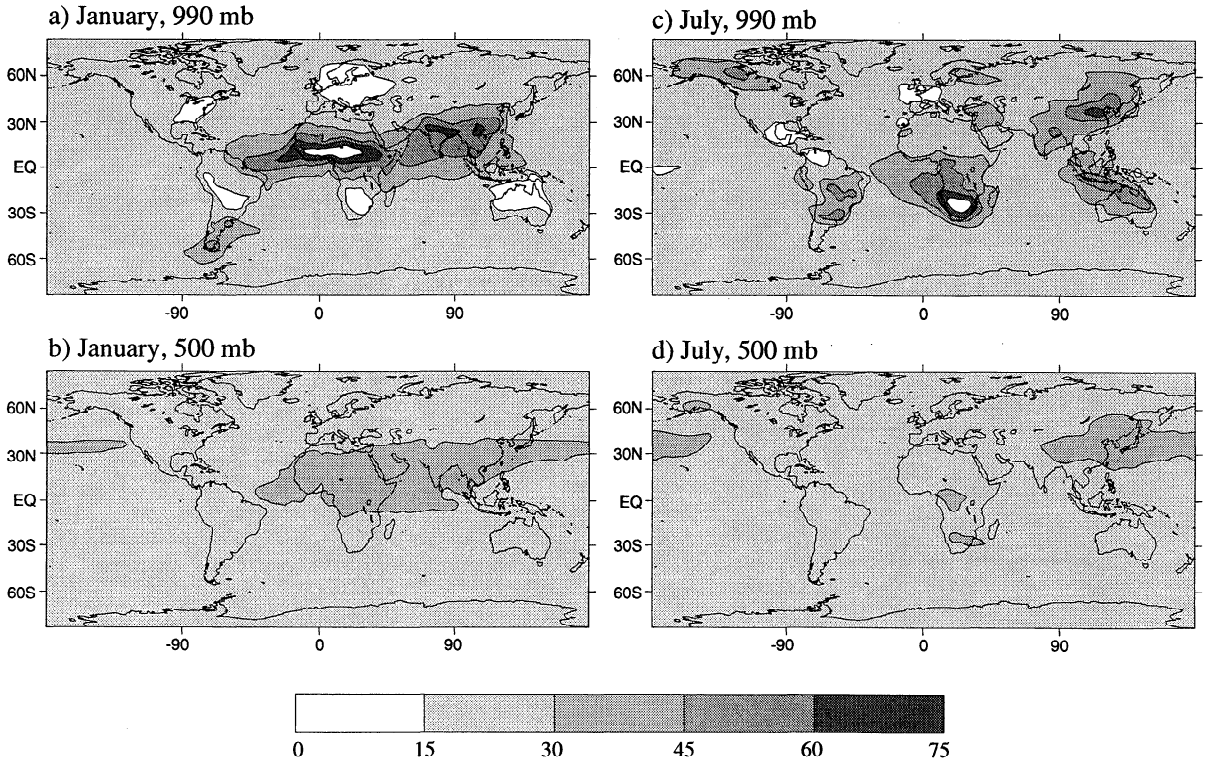

Figure 5. Percentage of total CO distribution from biomass burning (white within black denotes values greater than 75%). (a) January, 990 mbar. (b) January, 500 mbar. (c) July, 990 mbar. (d) July, 500 mbar.

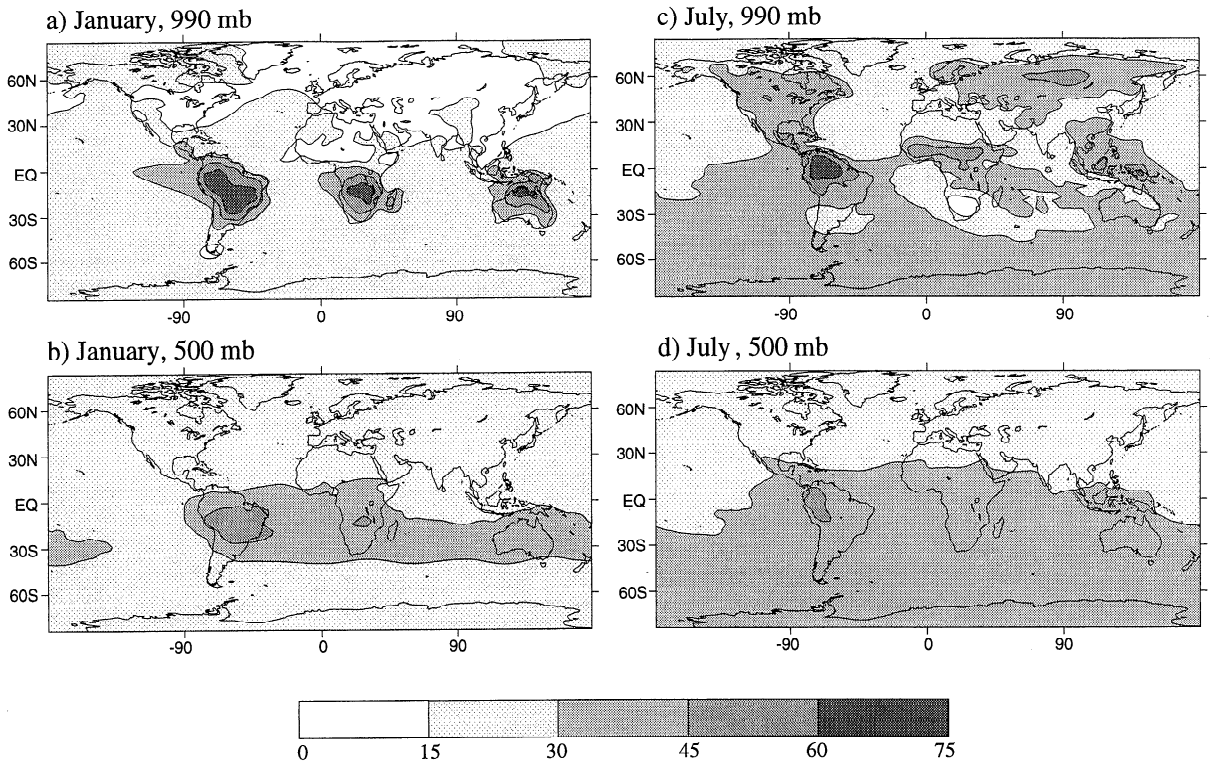

Figure 6. Percentage of total CO distribution from biogenic hydrocarbon oxidation. (a) January, 990 mbar. (b) January, 500 mbar. (c) July, 990 mbar. (d) July, 500 mbar.

westward with the trade winds at the surface, but reverses direction in the upper troposphere. In January the Intertropical Convergence Zone is south of the equator over regions of strong South American biogenic emissions. This high-CO air is convected to the upper troposphere where Southern Hemisphere midlatitude westerlies mix it toward the east. It should be noted that the plume of high-CO air from South America is significantly blocked at the surface by the Andes Mountains on the west coast of the continent. Thus the absolute concentrations of CO surface level air west of South America are relatively low (see Figure 3a), though the percent of this air reflecting a contribution from South American biogenic hydrocarbon oxidation is relatively high (Figure 6a). In July Northern Hemisphere biogenic emission regions are much stronger, though equatorial South America and Africa continue to account for the strongest CO emissions of this type. Although the Northern Hemisphere has more biogenic emission areas than the Southern Hemisphere, the high biogenic flux in South America and Africa, combined with the lack of fossil fuel emissions in the Southern Hemisphere, leads to a clear southern bias in the fraction of biogenic contribution at all levels.

The CO distribution from methane oxidation (not shown) displays a large degree of spatial homogeneity. Its fractional contribution is largest in areas with few other sources, such as the Southern Hemisphere oceans, and is a minimum near source regions and in the Northern Hemisphere during its winter.

5. Comparison with Data

Model data were compared with observations from the NOAA Climate Monitoring and Diagnostics Laboratory (NOAA/CMDL) cooperative flask sampling network from the Jungfraujoch station maintained by Swiss Federal Laboratories for Materials Testing and Research (EMPA), Duebendorf, and from the 10 NASA Global Tropospheре Experiment flight campaigns that measured CO. The NOAA/CMDL time series data were analyzed for the 33 ground-based sites from which CO data were available over the period June 1988 to December 1995 (time series length varies by site). Approximately once a week, air samples were collected in flasks and sent to Boulder, Colorado, to be analyzed using gas chromatography with mercuric oxide reduction detection [*Novelli et al.*, 1992; *Bakwin et al.*, 1994]. Measurements taken at Jungfraujoch were made continuously using ND-IR (non-dispersive infrared) technique with a commercially available instrument (Horiba APMA-360) and were compared to the National Institute of Standards and Technology (NIST) standard [*Zellweger et al.*, 2000; *Baltensperger et al.*, 1997; C. Zellweger, personal communication, 1999].

To compare with time series (NOAA/CMDL and EMPA) data, model time series were generated by sampling the model CO distribution at the gridbox corresponding to each sampling site. (The one exception to the procedure was in our comparison of model data with measurements from Key Biscayne, Florida. Because the model grid with which Key Biscayne actually corresponds contains metropolitan Miami and much of developed southern Florida, it was not felt to be an accurate comparison with Key Biscayne, which measures predominantly marine air masses. Instead, we compared measurements with model data from the next grid box to the southeast.) The altitude of each measuring station determined the model level with which data were compared. When station altitude corresponded with a single level height, that level was

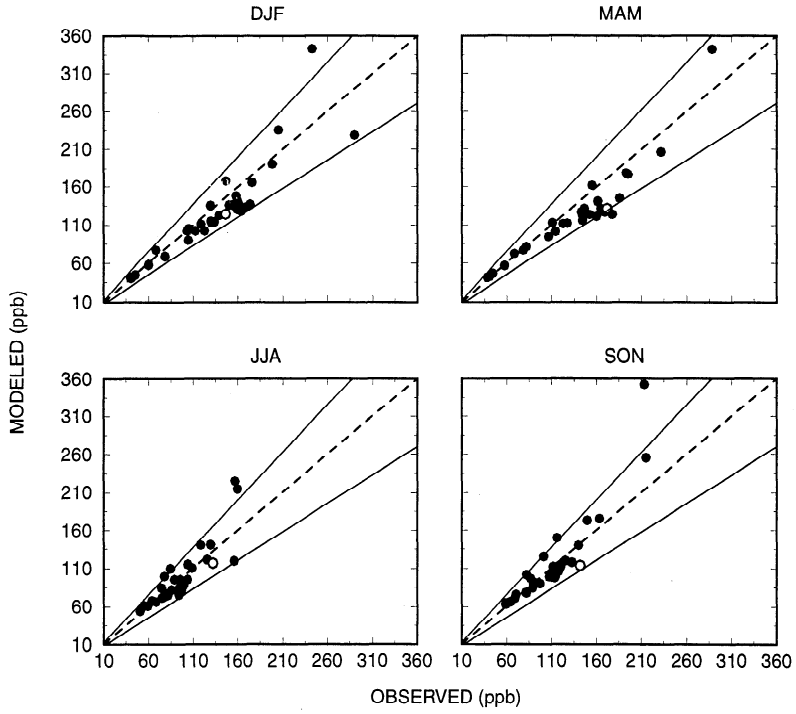

Figure 7. Seasonally averaged data points comparing model results with ground-based observations. Solid circles represent the NOAA/CMDL sites; open circles represent Jungfraujoch (EMPA) site; dashed lines denote 1:1 agreement between model and observations; solid lines denote ±25% bounds.

used for comparison. When station altitude fell between two model levels, the CO values at the adjacent levels were averaged based on the relative mass in each layer.

Monthly mean values of measurements were used for comparison. These mean values were calculated from the individual measurement data for NOAA/CMDL sites. In computing the monthly means, measurements designated as having problems in collection or analysis and measurements tagged by NOAA/CMDL as being nonrepresentative of background conditions were excluded. Data from EMPA were provided already averaged into monthly mean values. No detrending of the measured CO was performed, and only the NOAA/CMDL data were reported to the NOAA/CMDL CO scale.

As shown in Figure 7, the model compares well with surface observations. The scatterplot compares seasonally averaged model and observational data for all stations (solid lines denote 25%error bounds). We see that 93% of seasonal average data points fall within the 25% error limits.

Plates 1a-1h show time series for each of the 34 stations. These plots give the monthly average concentration of measured CO (purple circles) and GCTM results using our base case OH fields (black with squares). Each set of purple circles represents a different year of observed data, whereas the single set of black squares corresponds with the single year of model-simulated CO. In addition, time series for each of the single-source runs are shown: fossil fuel only (red), biomass burning only (green), biogenic hydrocarbon oxidation only (blue), and methane oxidation only (orange). These single source time series indicate the contribution of each source to the total simulated time series at that station. Measured yearly time series are shown individually to aid in model comparison. As model meteorology is that of a single representative year, it is most appropriate to compare the model distribution with observed values from individual years, rather than with the mean and standard deviation of all observed concentrations.

Aircraft data were taken from the ten NASA Global Tropospheric Experiment flights that measured CO: The Amazon Boundary Layer Experiment (ABLE 2A, ABLE 2B) [*Harriss et al.*, 1988, 1990]; The Arctic Boundary Layer Expedition (ABLE 3A, ABLE 3B) [*Harriss et al.*, 1992, 1994]; Chemical Instrumentation Test and Evaluation (CITE 2, CITE 3) [*Hoell et al.*, 1990, 1993]; Pacific Exploratory Mission-West (PEM-West A, PEM-West B) [*Hoell et al.*, 1997]; Pacific Exploratory Mission-Tropics [*Fuelberg et al.*, 1999]; and Transport and Atmospheric Chemistry Near the Equator - Atlantic (TRACE-A) [*Fishman et al.*, 1996]. To compare the data sets, flight data were binned into geographical regions (see Figure 8). Model data were averaged over each region and over the entire months in which the missions were flown. Since model

Plate 1. Time series data from CMDL compared with model results, all in ppb. Purple circles, monthly average measurements; black squares, model simulation with all sources; red, fossil fuel only; green, biomass burning only; blue, biogenic hydrocarbon oxidation only; orange, methane oxidation only. (a) Arctic, (b) North America and the North Atlantic, (c) South America and nearby tropical Atlantic, (d) Europe, (e) Africa and the Indian Ocean, (f) Asia, (g) Pacific Ocean, and (h) Antarctica and low southern latitudes.

a: Arctic

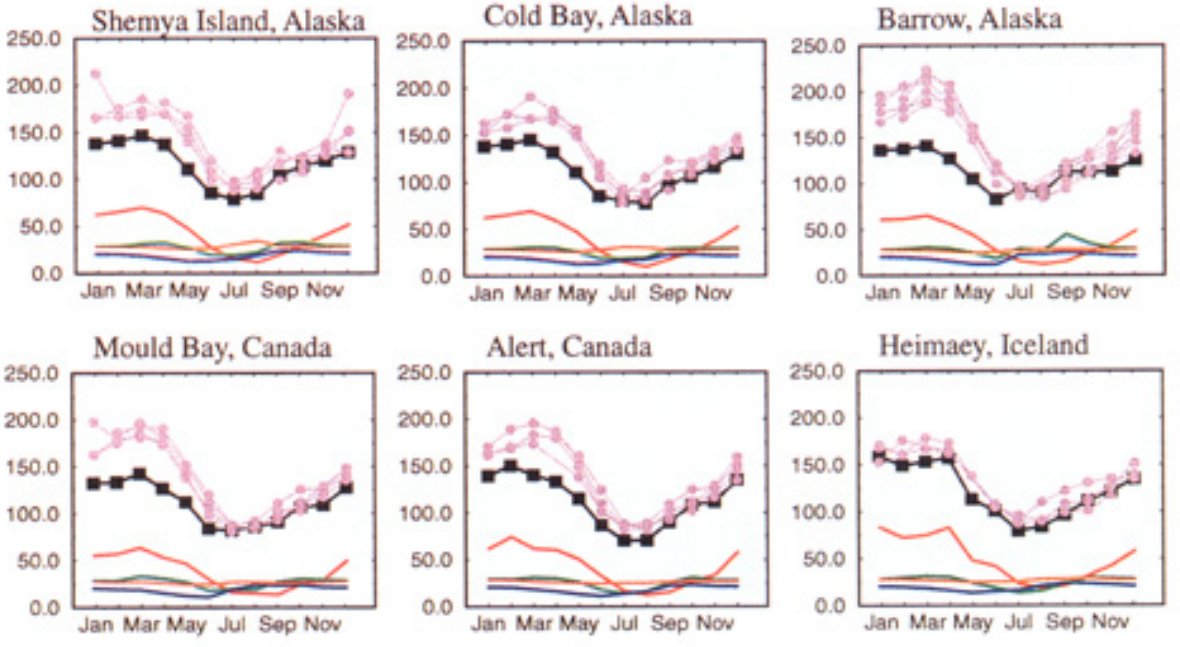

b: North America and the North Atlantic

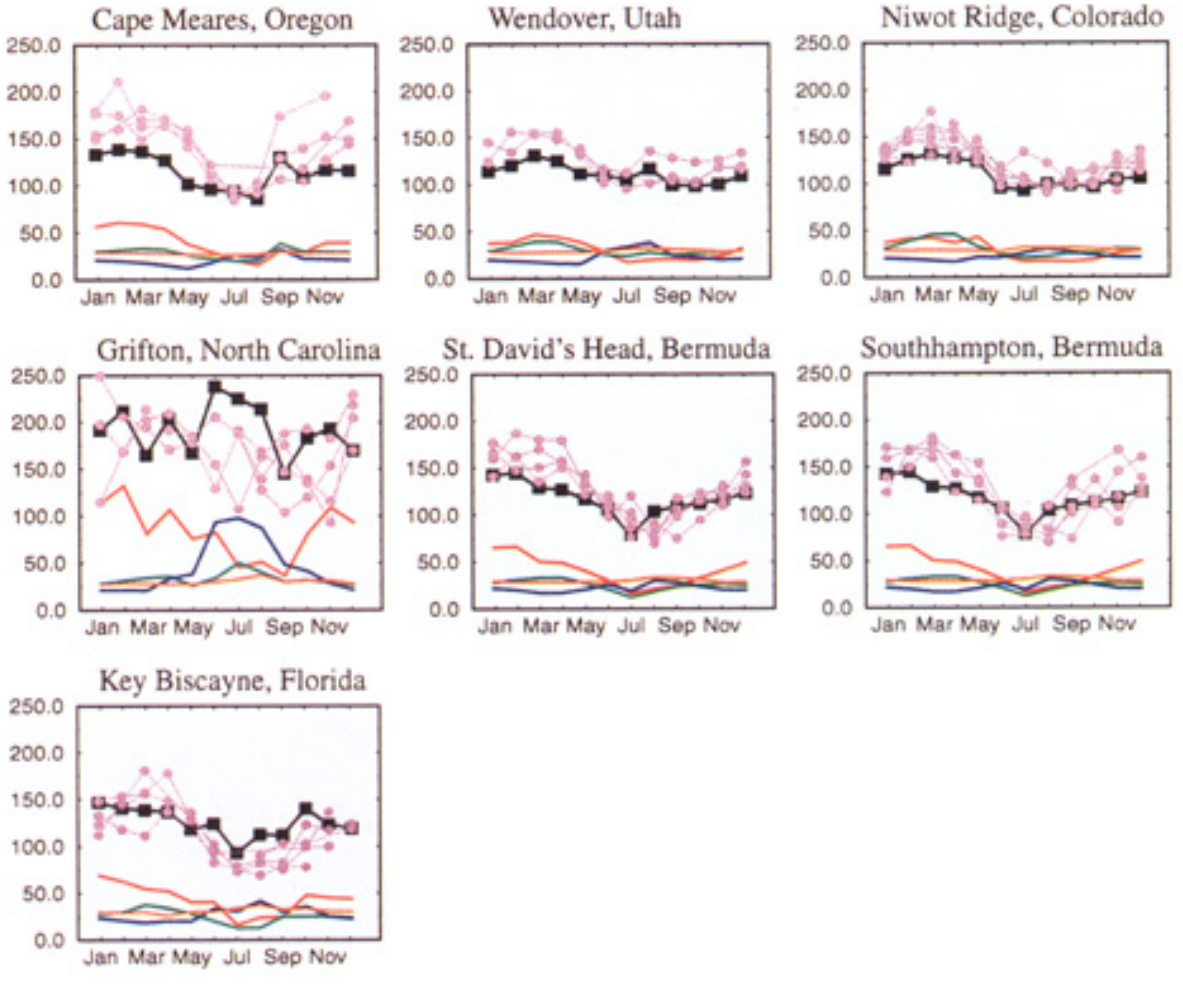

c: South America and Nearby Tropical Atlantic

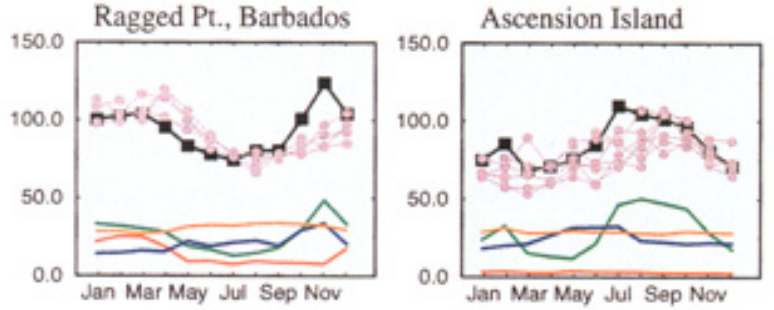

d: Europe

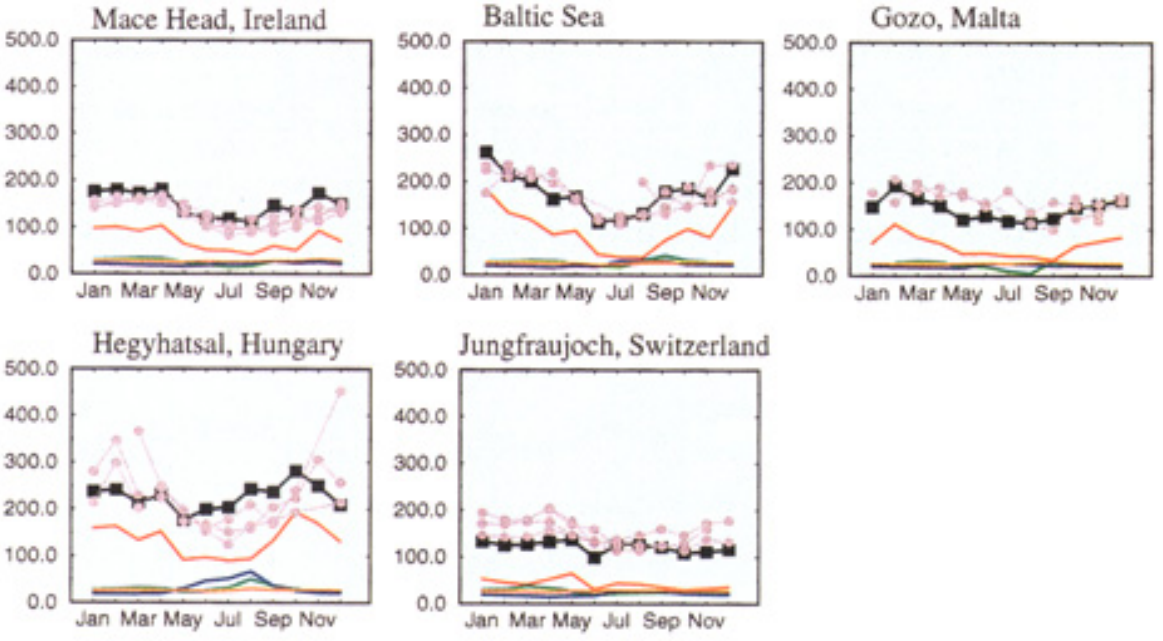

e: Africa and the Indian Ocean

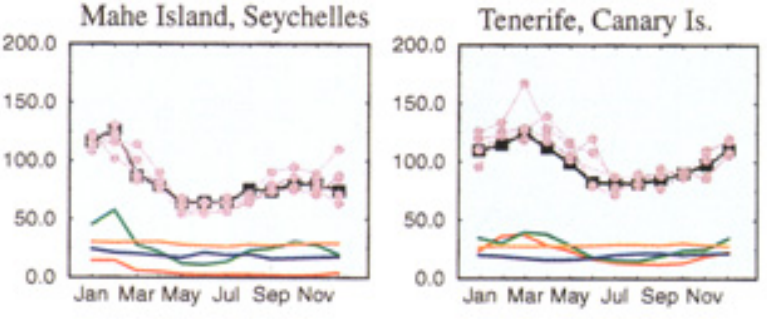

Plate 1. (continued)

f: Asia

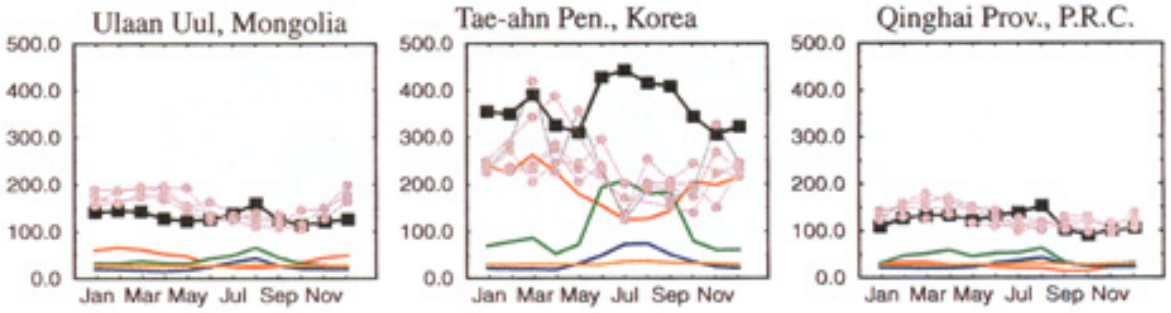

g: Pacific Ocean

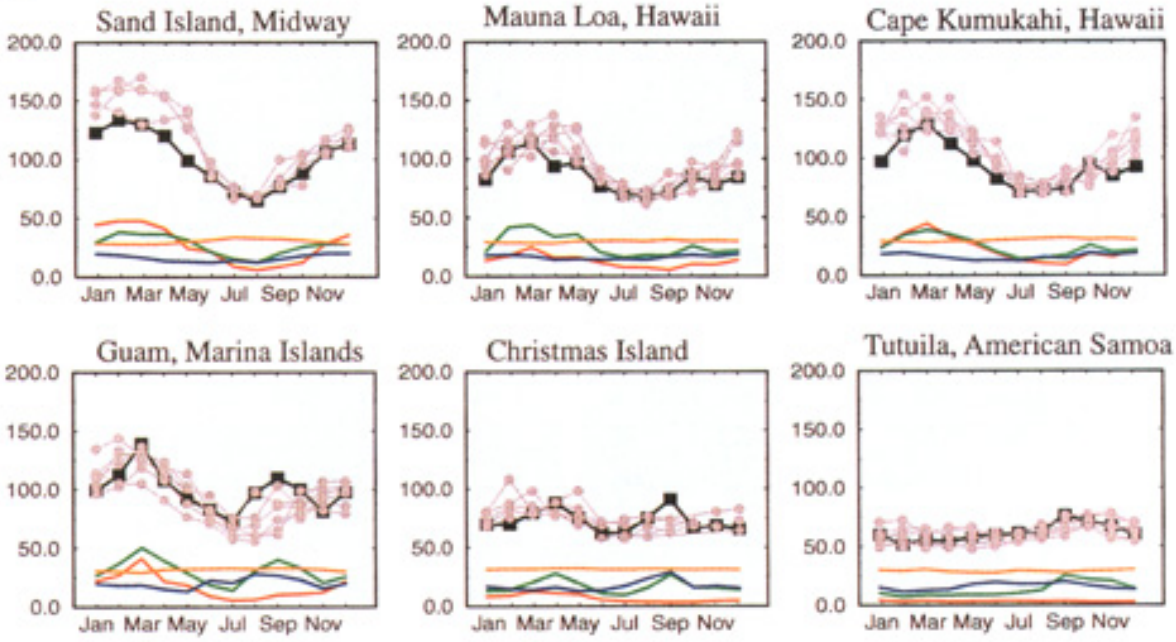

h: Antarctica and Low Southern Latitudes

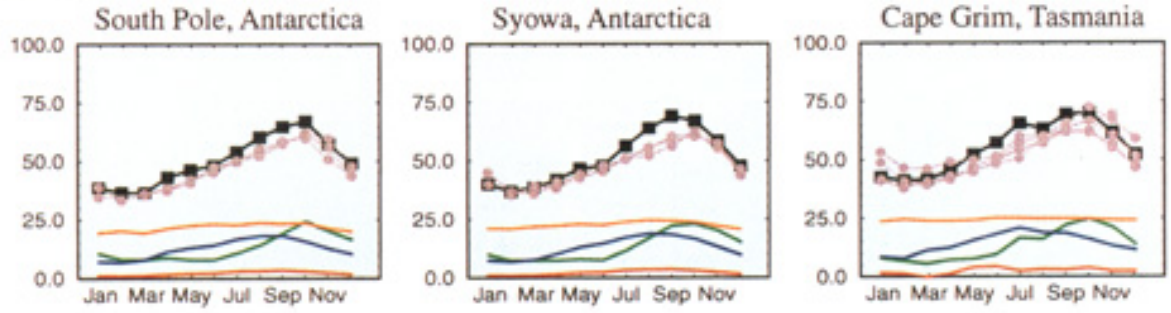

Plate 1. (continued)

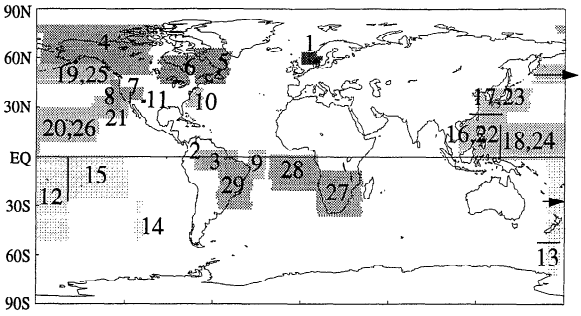

Figure 8. Regions for flight data comparison. 1, AASE 1 (not used); 2, ABLE 2A; 3, ABLE 2B; 4, ABLE 3A; 5, 6, ABLE 3B; 7, 8, CITE 2; 9, 10, CITE 3; 11, ELCHE (not used); 12, 13, 14, 15, PEM-Tropics A; 16, 17, 18, 19, 20, 21, PEM-West A (21 not used); 22, 23, 24, 25, 26, PEM-West B (26 not used); 27, 28, 29, TRACE-A (adapted from *Klonecki* [1999]).

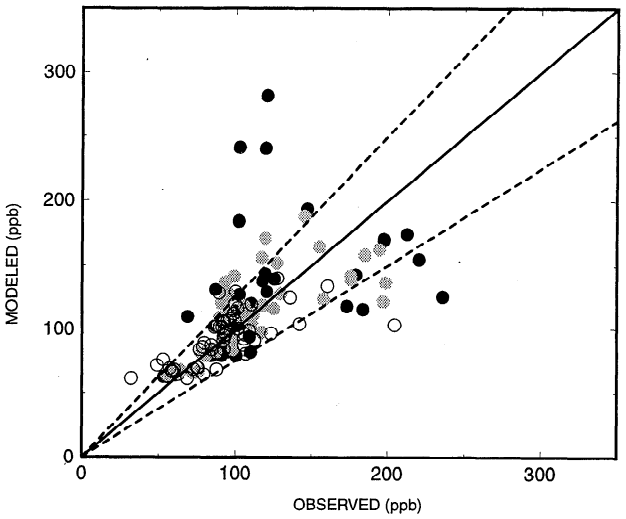

Figure 9. Regionally averaged data points comparing aircraft data from the NASA Global Tropospheric Experiment with model CO from base case run. Solid black circles denote points from 990 and 940 mbar; gray circles are points from 835 and 836 mbar; open circles are points from 500, 315, and 190 mbar; solid line denotes 1:1 agreement between model and observations; dashed lines denote ±25% bounds.

meteorology does not reflect specific events which occurred when a given data set was measured, it is most appropriate to average over reasonable temporal and spatial scales and compare mean values. Regions were selected based on flight paths and model meteorology [*Klonecki*, 1999]. For consistency with other studies, all 29 regions are shown in Figure 8, though only 25 have CO profiles for comparison.

In the sparsely sampled aircraft data one does not expect the same level of agreement seen in the time series data, given the scale over which model data are averaged for comparison. Rather, we use flight data to check for any systematic model bias. Figure 9 shows a scatterplot of observed CO values compared with model data. The plot has one point per level for each region relevant to each flight campaign. Thus observed values include the mean of all samples taken in a particular region at a particular height during a campaign. As stated, model data for these points are the average of model values over the region during the months during which each mission occurred for each level. For the 144 data points compared (25 regions, each with 4 to 7 vertical levels), 79% fall within the 25% error bounds. Solid black circles denote points from 990 and 940 mbar; gray circles are points from 835 and 836 mbar; open circles are points from 500, 315, and 190 mbar. Although, overall, model CO does not show a systematic bias when compared with aircraft data, high-altitude measurements (open circles) exhibit a somewhat low bias at high concentrations, and high-CO points scatter beyond the 25% error bounds. The largest differences between model and aircraft

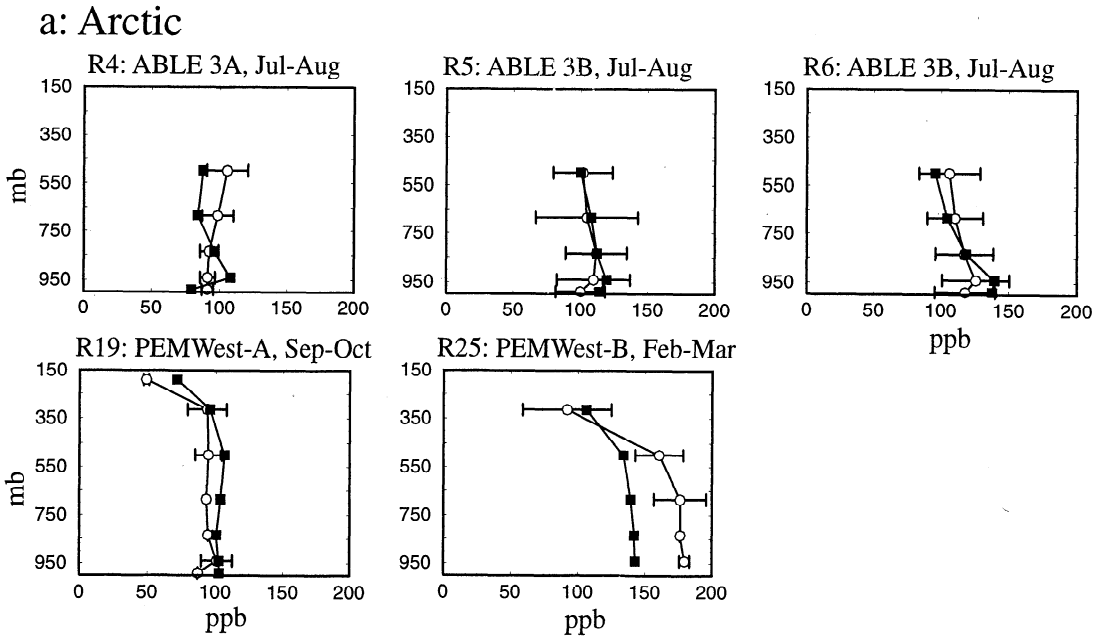

Figure 10. Profiles from aircraft data compared with model results. Open circles, regional average measurements, with standard deviations; solid squares, model simulation with base case OH fields.

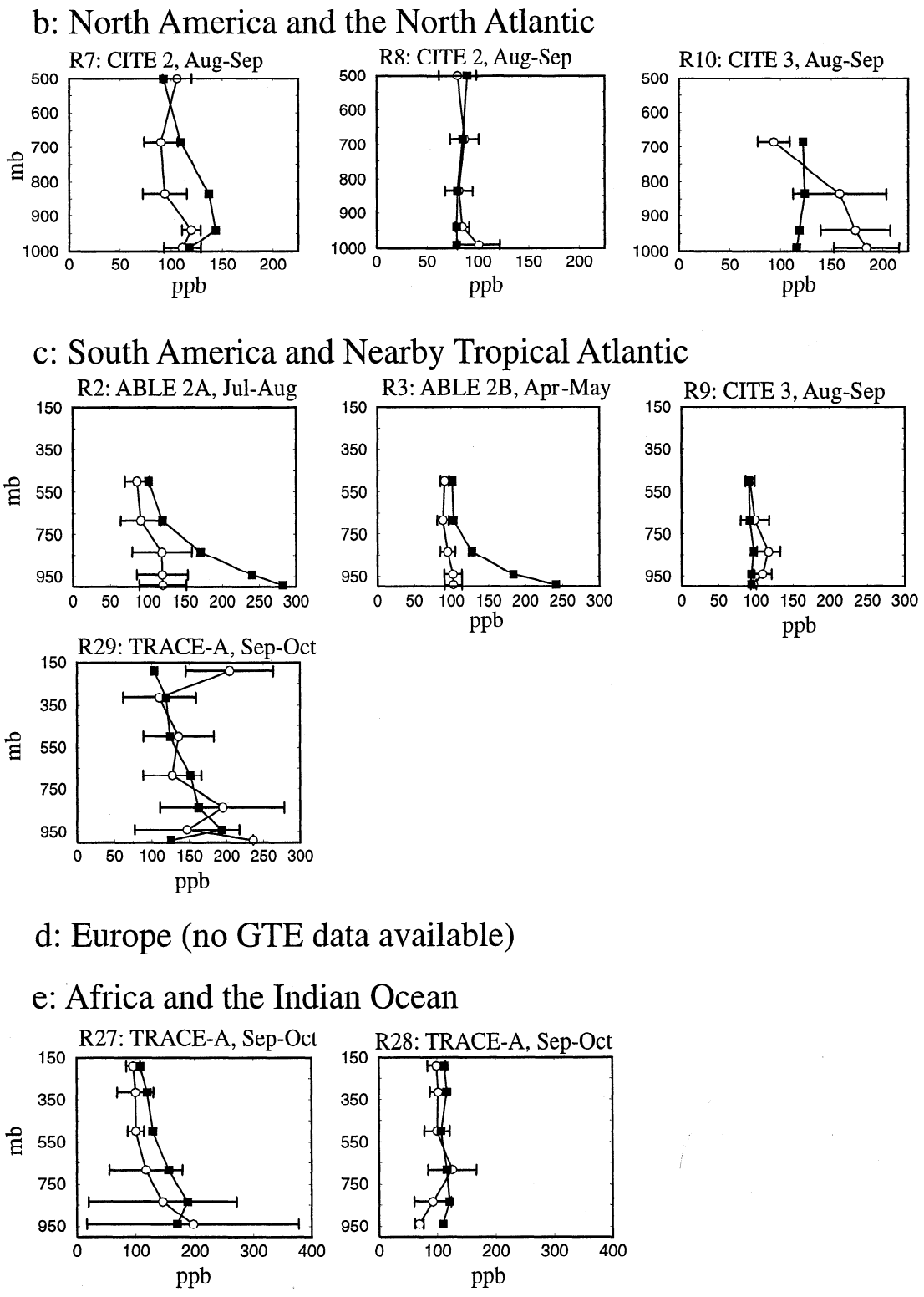

Figure10. (continued)

data occur in the lowest two model levels, with agreement improving at higher levels and lower CO values.

Mean vertical CO profiles for individual regions are shown in Figure 10. The individual profiles should not be used for evaluating model accuracy since the quantities being compared are fundamentally different: spatially and temporally limited samples of the CO distribution from the data, versus a complete time and regional mean of model conditions. To avoid any confusion, we have omitted standard deviations from model profiles. Rather, the mean values are presented to illustrate the trends in model and aircraft data summarized in the scatterplot (Figure 9) to show that the model has no systematic high or low bias in vertical gradient and to point out specific patterns relevant to the regional discussion of carbon monoxide presented below.

CO behavior described by GCTM results and measure-

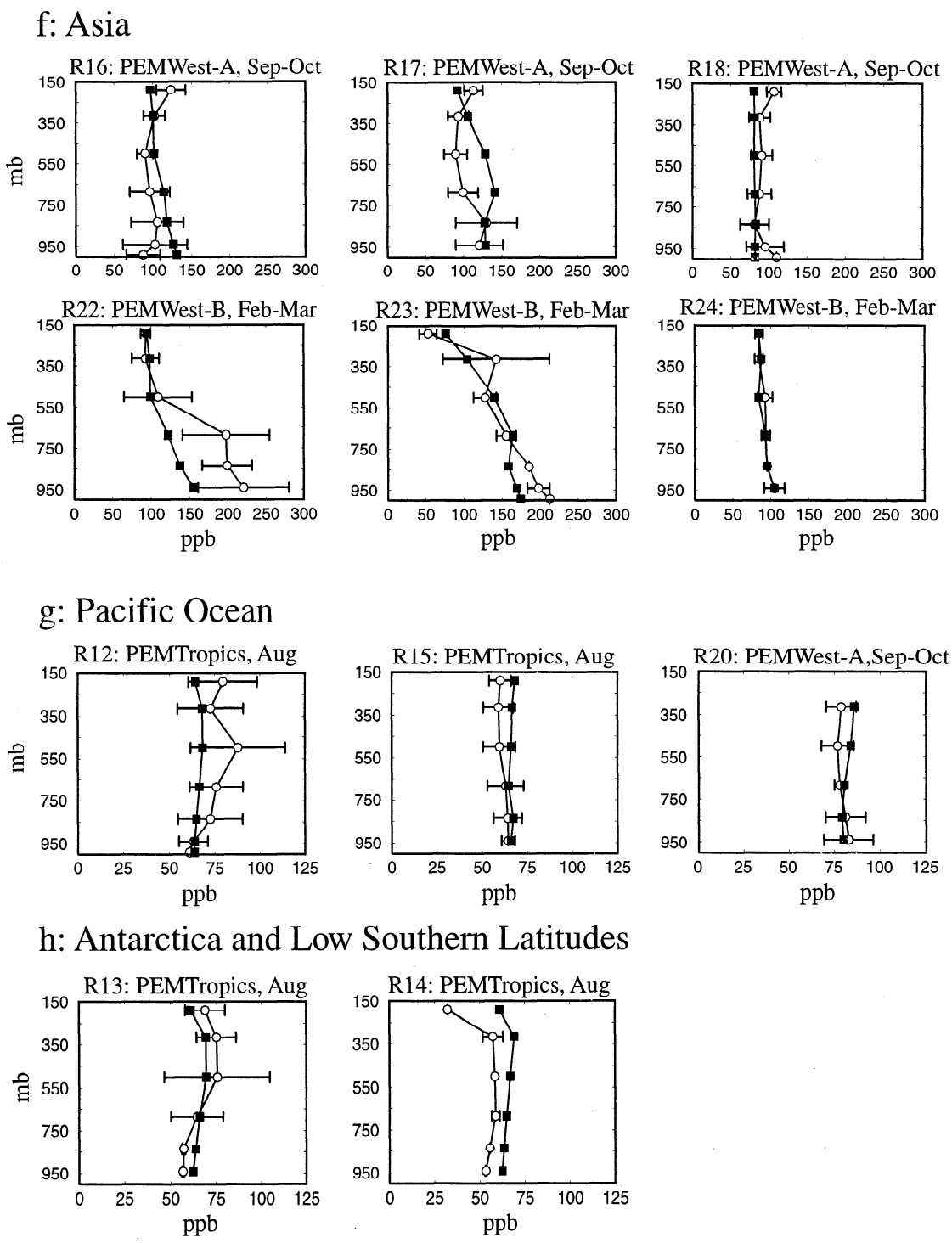

Figure 10. (continued)

ments will be discussed in the context of each of the following regions: Arctic, North America and North Atlantic, South America and nearby tropical Atlantic, Europe, Africa and Indian Ocean, Asia, Pacific, and Antarctica and low southern latitudes.

5.1. Arctic

Winter high-latitude regions receive low levels of solar radiation, leading to low OH concentrations. Thus the lifetime of CO in the Arctic is very long, and its distribution well-mixed. Fossil fuel is by far the largest emission type in the Northern Hemisphere winter, so this source controls the composition of CO throughout the Arctic winter. In the summer the contribution from fossil fuel derived CO relative to the total CO distribution decreases as the lifetime of CO over continental source regions drops to about 15 days.

In comparing model results with observations at the six arctic sites (Plate 1a, Table 2), Shemya Island, Alaska; Cold Bay, Alaska; Barrow, Alaska; Mould Bay, Northwest Territories, Canada; Alert, Northwest Territories, Canada; Heimaey,

Table 2. Surface Measurement Sites

Site	Latitude and Longitude	Altitude, M	Time Period	Contributor
		Arctic		
Shemya Island, Alaska	52°43'N, 174°06'E	40	Oct. 1990 to Dec. 1995	NOAA/CMDL
Cold Bay, Alaska	55°12'N, 162°43'W	25	Nov. 1990 to Dec. 1995	NOAA/CMDL
Barrow, Alaska	71°19'N, 156°36'W	11	July 1988 to Dec. 1995	NOAA/CMDL
Mould Bay, Canada	76°15'N, 119°21'W	58	Nov. 1990 to Dec. 1995	NOAA/CMDL
Alert, Canada	82°27'N, 62°31'W	210	Oct. 1990 to Dec. 1995	NOAA/CMDL
Heimaey, Iceland	63°15'N, 20°09'W	100	Oct. 1992 to Nov. 1995	NOAA/CMDL
		North America		
Cape Meares, Oregon	45°29'N, 123°58'W	30	Nov. 1990 to Dec. 1995	NOAA/CMDL
Wendover, Utah	39°54'N, 113°43'W	1320	May 1993 to Dec. 1995	NOAA/CMDL
Niwot Ridge, Colorado	40°03'N, 105°35'W	3475	Dec. 1988 to Dec. 1995	NOAA/CMDL
Grifton, North Carolina	35°21'N, 77°23'W	505	July 1992 to Dec. 1995	NOAA/CMDL
St. David's Head, Bermuda	32°22'N, 64°39'W	30	Nov. 1990 to Dec. 1995	NOAA/CMDL
Southhampton, Bermuda	32°16'N, 65°53'W	30	Nov. 1990 to Dec. 1995	NOAA/CMDL
Key Biscayne, Florida	25°40'N, 80°12'W	3	Nov. 1990 to Dec. 1995	NOAA/CMDL
		South America and Tropical Atlantic		
Ragged Point, Barbados	13°10'N, 59°26'W	3	Dec. 1990 to Dec. 1995	NOAA/CMDL
Ascension Island, Atlantic Ocean	7°55'S, 14°25'W	54	Feb. 1989 to Dec. 1995	NOAA/CMDL
		Europe		
Mace Head, Ireland	53°20'N, 9°54'W	25	June 1991 to Dec. 1995	NOAA/CMDL
Baltic Sea	55°30'N, 16°40'E	7	Aug. 1992 to Dec. 1995	NOAA/CMDL
Gozo, Malta	36°03'N, 14°11'E	30	Oct. 1993 to Dec. 1995	NOAA/CMDL
Hegyhatsal, Hungary	46°58'N, 16°23'E	240	March 1993 to Dec. 1995	NOAA/CMDL
Jungfraujoch, Switzerland	46°33'N, 7°59'E	3580	April 1996 to July 1999	EMPA
		Africa and the Indian Ocean		
Mahe Island, Seychelles	04°40'S, 55°10'E	3	Nov. 1990 to Dec. 1995	NOAA/CMDL
Tenerife, Canary Islands	28°18'N, 16°29'W	2300	Nov. 1991 to Dec. 1995	NOAA/CMDL
		Asia		
Ulaan Uul, Mongolia	44°27'N, 111°06'E	914	Jan. 1992 to Dec. 1995	NOAA/CMDL
Tae-ahn Peninsula, Korea	36°44'N, 126°08'E	20	Nov. 1990 to Dec. 1995	NOAA/CMDL
Qinghai Province, China	36°16'N, 100° 55'E	3810	Aug. 1990 to Dec. 1995	NOAA/CMDL
		Pacific		
Sand Island, Midway	28°13'N, 177°22'W	4	Nov. 1990 to Dec. 1995	NOAA/CMDL
Mauna Loa, Hawaii	19°32'N, 155°35'W	3397	July 1989 to Dec. 1995	NOAA/CMDL
Cape Kumukahi, Hawaii	19°31'N, 154°49'W	3	July 1989 to Dec. 1995	NOAA/CMDL
Guam, Marina Islands	13°26'N, 144°47'E	2	Oct. 1989 to Dec. 1995	NOAA/CMDL
Christmas Island	1°42'N, 157°10'W	3	Dec. 1989 to Dec. 1995	NOAA/CMDL
Tutuila, American Samoa	14°15'S, 170°34'W	42	Sept. 1989 to Dec. 1995	NOAA/CMDL
		Antarctica and Low Southern Latitudes		
South Pole, Antarctica	89°59'S, 24°48'W	2810	Dec. 1989 to Dec. 1995	NOAA/CMDL
Syowa, Antarctica	69°0'S, 39°35'E	11	Feb. 1990 to Dec. 1995	NOAA/CMDL
Cape Grim, Tasmania	40°41'S, 144°41'E	94	Nov. 1990 to Dec. 1995	NOAA/CMDL

Vestmannaeyjar, Iceland, we see that the model underestimates the spring peak in CO levels at all sites except Iceland. The probable cause of this discrepancy is unrealistically strong downward transport from the lower stratosphere and insufficient ventilation by baroclinic waves in the model's high northern latitudes. Model results simulating global ozone distribution support this assessment: In the winter, Northern Hemisphere high-latitude ozone concentrations are greater than observed, as would be expected from overly intense downward transport (W. J. Moxim, personal communication, 1998). This springtime underestimation also suggests that our fossil fuel emission fields are unrealistically low, contributing to the discrepancies with observations. At Iceland the close correspondence between model and observations may be due to the station's lower latitude or the influence of fossil fuel emissions from Europe (Figure 4a).

Aircraft data from Arctic flights is compared in regions R4, R5, R6, R19, and R25 (Figure 10, Table 3). The Arctic

Table 3. Aircraft Measurement Regions

Region ID	Mission	Latitude and Longitude	Time Period
		Arctic	
R4	ABLE 3A	175°W-105°W, 50°N-80°N	July-Aug. 1988
R5	ABLE 3B	72°W-52°W, 45°N-65°N	July-Aug. 1990
R6	ABLE 3B	95°W-77°W, 45°N-65°N	July-Aug. 1990
R19	PEM-West A	160°E-130°W, 45°N-55°N	Sept.-Oct. 1991
R25	PEM-West B	160°E-130°W, 45°N-55°N	Feb.-March 1994
		North America	
R7	CITE 2	125°W-110°W, 35°N-40°N	Aug.-Sept. 1986
R8	CITE 2	130°W-125°W, 30°N-45°N	Aug.-Sept. 1986
R10	CITE 3	77°W-69°W, 31°N-41°N	Aug.-Sept. 1989
		South America and Tropical Atlantic	
R2	ABLE 2A	70°W-45°W, 8°S-2°N	July-Aug. 1985
R3	ABLE 2B	65°W-45°W, 6°S-EQ	April-May 1987
R9	CITE 3	77°W-9°W, 31°N-41°N	Aug.-Sept. 1989
R29	TRACE-A	55°W-35°W, 30°S-5°S	Sept.-Oct. 1992
		Africa and the Indian Ocean	
R27	TRACE-A	12°E-40°E, 35°S-10°S	Sept.-Oct. 1992
R28	TRACE-A	20°W-10°E, 20°S-EQ	Sept.-Oct. 1992
		Asia	
R16	PEM-West A	110°E-140°E, EQ-30°N	Sept.-Oct. 1991
R17	PEM-West A	110°E-155°E, 30°N-40°N	Sept.-Oct. 1991
R18	PEM-West A	140°E-180°E, EQ-20°N	Sept.-Oct. 1991
R22	PEM-West B	110°E-140°E, EQ-30°N	Feb.-March 1994
R23	PEM-West B	110°E-155°E, 30°N-40°N	Feb.-March 1994
R24	PEM-West B	140°E-180°E, EQ-20°N	Feb.-March 1994
		Pacific	
R12	PEM-Tropics A	170°E-160°W, 50°S-EQ	Aug. 1996
R15	PEM-Tropics A	160°W-120°W, 25°S-EQ	Aug. 1996
R20	PEM-West A	180°W-140°W, 10°N-30°N	Sept.-Oct. 1991
		Antarctica and Low Southern Latitudes	
R13	PEM-Tropics A	171°E-173°E, 73°S-45°S	Aug. 1996
R14	PEM-Tropics A	111°W-109°W, 50°S-28°S	Aug. 1996

For Europe, no GTE data are available.

Boundary Layer Expedition flights (R4, R5, R6) were flown in July and August. As shown in the time series data (Plate 1a), CO reaches a minimum during these summer months. In all three areas the profile is relatively uniform with height because this summertime CO is composed of well-mixed contributions from all four sources. Regions R19 and R25 reflect data taken as part of the PEM-West A (September-October) and PEM-West B (February-March) campaigns, respectively. Over this North Pacific region both model and observations indicate lowest values in the upper troposphere (Figure 10).

5.2. North America and North Atlantic

During winter the most significant North American source is fossil fuel, which dominates over the long-lived CO from biomass burning, biogenic emissions, and oxidized methane. During this time the CO pool from the eastern United States extends out over the Atlantic and, due to its long lifetime, mixes well throughout the mid and high latitudes. Most of the western half of the continent experiences the well-mixed background levels seen at the Arctic.

During the summer the situation is more complicated. Increased continental convection creates a plume of high CO air off the eastern United States, which is lifted and mixes at higher altitudes. Meanwhile, methane oxidation, biogenic emissions, and biomass burning (the latter two of which are concentrated in the southeastern United States and northwestern Canada, but which extend over the bulk of the continent) contribute to a summer rise in sources, just as the rise in OH concentration increases the sinks.

At all seven monitoring stations in North America or the nearby Atlantic (Plate 1b, Table 2), Cape Meares, Oregon; Wendover, Utah; Niwot Ridge, Colorado; Grifton, North Carolina; St. David's Head, Bermuda; Southhampton, Bermuda; and Key Biscayne, Florida, CO from fossil fuel plays a major role in governing seasonality, though the magnitude of its contribution varies by location. In comparing the time series from the model simulation with all sources with those from the simulation with only fossil fuel (red line on plots, Plates 1a-1h), one sees that most seasonal patterns shown by CO from fossil fuel mirror those of the full distribution. Varia-

tions in CO from fossil fuel arise only from changes in transport and hydroxyl concentrations, since fossil fuel emissions are assumed to have no seasonal cycle in North America.

At most North American and North Atlantic sites, model agreement with observation is good, both in magnitude and seasonality. However, two types of problems are seen: too much CO in the southeastern United States and too little at some western sites. In the southeastern United States, measured at Grifton, North Carolina and Key Biscayne, Florida, summer biogenic emissions appear too high. Time series from Grifton, where both biogenic and fossil fuel emissions are very high, predictably displays a complex behavior. The overall CO signal appears highly fluctuating, both in the model and in observations due to monthly variations in transported fossil fuel CO. As fossil fuel emissions in North America are assumed to have no seasonality, the magnitude of the contribution from this source wanes in summer when OH concentrations are high. During this same time, biogenic emissions peak. The increase in biogenic hydrocarbon oxidation is much greater than the increase in destruction by summertime hydroxyl concentrations, so the fractional contribution of this source rises just as the contribution from fossil fuel drops. While the observations show a high degree of interannual as well as monthly variability, the summertime biogenic peak is not observed. Higher model values during the summer months in Key Biscayne also appear attributable to biogenic hydrocarbon oxidation. Thus these sites indicate that biogenic hydrocarbon oxidation is too high in the southeastern United States. The underestimation of springtime CO in the western United States, especially at Cape Meares, Oregon, and Wendover, Utah, may be due to an underestimate of the transport of both biomass burning and fossil fuel burning emissions across the Pacific from Asia. It is this transpacific transport which accounts for the spring peak in biomass CO at these western sites (indicated by the green lines in Plates 1a-1h). An additional factor, however, may well be that overall fossil fuel emissions in the Northern Hemisphere are too low.

Regions R7, R8, and R10 represent North American air masses (Figure 10, Table 3). Region 10 shows a model profile differing sharply from the observations, with higher values seen in the observed profile. This observed R10 data were taken during a summertime CITE campaign off the east coast of the United States. The GCTM's summertime circulation establishes a strong Bermuda High which prevents the transport of simulated U.S. pollution during late July and August, while the actual circulation, which does establish a strong Bermuda High during some summers, did not do so during the CITE-3 measurement period. Owing to these meteorological differences, higher NO_x concentrations were also observed in this same region [*Levy et al.*, 1999].

5.3. South America and Tropical Atlantic

Biogenic emissions account for the majority of emitted CO from South and Central America, with biomass burning as the next highest contributor. Easterly trade winds carry emissions from tropical latitudes out toward the Pacific, while the tropical Atlantic sees the distinct mark of biomass burning from Africa. Although we do not have any time series data from areas downwind of South American emissions (midlatitude Southern Atlantic and nearby tropical Pacific), flights from the ABLE 2A, ABLE 2B, CITE 3, and TRACE-A all measure air masses reflecting South American emissions (Figure 10). Measurements from the nearby tropical Atlantic include time series data from Ragged Point, St. Phillip's Parish, Barbados, and Ascension Island, Atlantic Ocean (Table 2).

Agreement with ground observations is fairly good (Plate 1c), though Barbados shows a peak due to biomass burning which is not observed, a possible indicator of incorrect biomass burning timing in northern Africa. At the equator the contribution of fossil fuels to the total CO drops off rapidly. Whereas the magnitude of fossil fuel CO contribution at Barbados is comparable to all other three sources (25 ppb in January-March), at Ascencion (at about 8°S), fossil fuel is negligible, with biomass burning determining seasonality and biogenic and methane emissions together contributing over half of the total magnitude.

The aircraft data from R2 and R3 may indicate a model overabundance of CO at low levels over the Amazon (Figure 10, Table 3). The low concentrations of observed values near the surface reflect much cleaner air than is found over this biogenic and biomass burning source region in the model. The discrepancy may indicate an overestimation of CO from biogenic hydrocarbon oxidation or inaccuracies in the timing of the biomass burning source. Individual flight profiles taken during the dry season by the ABLE 2A mission (not shown, but average values shown in R2) reflect much higher CO values measured at the end of the mission (200 ppb and higher from ground to 3 km) than measured at the beginning (75-95 ppb). This increase in measured values is considered to be biomass burning related [*Sachse et al.*, 1988], with data from later flights agreeing more closely with the average model values over the region. Profiles from R9, just off the east coast, and R29, over Brazil, do not show enhanced boundary layer values in either the model or the observations (Figure 10, Table 3).

5.4. Europe

The behavior of CO over Europe resembles that of the eastern United States. Both regions have large fossil fuel emissions; Europe's maximum emitting area reaches from the United Kingdom across Germany to Poland, and southward to northern Italy (Figure 1a). Midlatitude westerlies spread the CO pool created by these emissions eastward, especially in winter, when the lifetime is longer and convection is weaker. The eastward extension of the emissions from Europe is more pronounced than that over North America in part because Europe's higher latitude leads to a longer CO lifetime, in part because high emission levels persist eastward through Russia. During the winter, emissions from biomass burning and biogenic hydrocarbons are very low. These two emission sources increase in summer, but remain dwarfed by the fossil fuel source.

The four sites from which NOAA/CMDL measurement data are available border industrialized Europe (Plate 1d, Table 2). To the northwest is Mace Head, Ireland; to the north is the Baltic Sea; to the south is Gozo, Malta; and to the east is Hegyhatsal, Hungary. The model agrees fairly well with observations at Mace Head, the Baltic Sea, and Gozo, but overestimates CO during the summer in Hungary. At all sites, fossil fuel strongly dominates the source composition.

Ground-based measurement data were also available from EMPA, Duesendorf (C. Zellweger, personal communication, 1999) taken in Jungfraujoch, Switzerland (Table 2). Although we capture the seasonality of the signal at Jungfraujoch, we tend to underestimate the overall CO signal. This low bias likely arises from the low fossil fuel source used in our simu-

lation. Although most other sites in Europe do not exhibit this underestimation, the CO measured at Jungfraujoch's high altitude reflects less the local emissions and more the longer-lived CO resulting from many Northern Hemisphere sources. No GTE aircraft data were available for comparison in Europe.

5.5. Africa and the Indian Ocean

As in South America, biomass burning and biogenic emissions are large throughout Africa, creating a major tropical and Southern Hemisphere CO source. Biomass burning occurs through parts of northern Africa from October through April, and in equatorial and southern Africa from June through November. Because the African continent is located between 30°N and 30°S, most of its emissions throughout the year are carried westward over the Atlantic by the trade winds.

The observing station at Mahe Island, Seychelles, is located just south of the equator in the western part of the Indian Ocean, with concentrations below 90 ppb through most of the year due to its upwind location from high source regions. In February, however, burning in the Guinea Savanna and equatorial African regions leads to a pronounced peak in both the model and observations. Tenerife, Canary Islands, in the Atlantic reflects biomass burning from Africa and a background fossil fuel contribution (Piate 1e, Table 2).

Data from the TRACE-A campaign were compared with the model in R27 and R28 over southern Africa (Figure 10, Table 3). The vertical profiles reflect similar shape and magnitude for both regions.

5.6. Asia

In January, the region of high (200-500 ppb) surface level CO extends over India, the southern half of China down through Indonesia, as well as over Korea and Japan (Figure 3). This distribution shifts northward by July, at which time high CO is concentrated with peak values in the northeast third of China, the Korean Peninsula, and Japan. CO from oxidation of biogenic hydrocarbons forms in Indonesia and Indochina year-round, with the source region spreading to China in the summer months and peaking in India during September; fossil fuel emission maxima occur in northeast China, Korea, and Japan; CO from methane, as discussed, is extremely well-mixed, contributing 25-35 ppb with a very weak seasonal cycle. Biomass burning emissions strongly influence the overall CO distribution in the region. The burning season for Indonesia runs from July through October, and in Southeast Asia and India it runs from January through May. In addition, these regions burn biofuels year-round.

Three observing sites are used to diagnose model performance in Asia (Plate 1f, Table 2): Ulaan Uul, Mongolia; Tae-ahn Peninsula, Korea; and Qinghai Province, China, just west of the developed northeastern region. The Tae-ahn Peninsula reflects overly high model values all year, with differences of 100 to 200 ppb from June through October. The sharp summer biomass burning peak in the model simulation of CO at the Tae-ahn Peninsula is also likely due to unrealistic advective transport. During the summer months the model displays a low-pressure system over continental Asia just inland from the Sea of Japan. The resulting cyclonic circulation advects the summer biomass burning emissions in northern China southeastward to the Korean Peninsula. This low-pressure system is not seen in observed data; rather, the peninsula is flushed with marine air from the southerly surface winds through much of the summer season. At other Asian sites the model simulates observed values well, but shows a small overestimation in CO from biomass burning in July, and a slight underestimation of springtime values.

Aircraft data from PEM-West A (September-October) and B (February-March) flights east of Asia were compared with the model in Figure 10 (Table 3). We agree reasonably well in profile shape and magnitude for all regions except R22, where observed values are about 75 ppb higher than the spatial-temporal CO model mean in that region.

5.7. Pacific Ocean

Although the western Pacific Ocean feels the impact of Asian emissions, most of the basin sees only the well-mixed contribution of CO from all four sources. As such, CO from fossil fuel has a north-south gradient, biomass burning and biogenic hydrocarbon oxidation are higher in the Northern Hemisphere during the winter, but roughly equal between the two hemispheres in the summer, and methane shows a very weak gradient from the tropics to the poles.

Six observing stations are located in the Pacific (Plate 1g, Table 2). From north to south these are as follows: Sand Island, Midway; Mauna Loa, Hawaii; Cape Kumukahi, Hawaii; Guam, Marina Islands; Christmas Island; and Tutuila, American Samoa. At Midway the spring CO maximum is underestimated in the model. Since the springtime maximum is due to transport from Asia, and a similar underestimate is observed in the comparison of spring timeseries values from the western United States, we may conclude that the model transports unrealistically small quantities of CO westward from Asia. This underestimation of CO at Midway lends further evidence that our fossil fuel emissions are too low in much of the Northern Hemisphere, and particularly in Asia. The two stations at Hawaii, Cape Kumukahi and Mauna Loa, sample boundary layer air and the free troposphere, respectively. In the boundary layer, fossil fuel from local sources contributes a CO fraction nearly equivalent to biomass burning in magnitude and seasonality. Higher up, at the Mauna Loa station, biomass burning emissions primarily control the observed distribution, especially in winter. The model captures the behavior at both levels well. Vertical profiles from R12, R15, and R20 (Figure 10, Table 3) reflect that Pacific CO concentrations are well-mixed with height in both measurements and the model.

5.8. Antarctica and Low Southern Latitudes

At all low southern latitudes, methane oxidation dominates the magnitude of the observed signal, with biomass burning and biogenic emissions combining to govern seasonality (Plate 1h, Table 2). The three observing sites, South Pole, Antarctica; Syowa, Antarctica; and Cape Grim, Tasmania, all exhibit similar patterns. The model slightly overestimates CO concentrations, especially during times of high CO from biomass and biogenic emissions. This difference may be due to the CO yield assumed in our methane oxidation calculation. If only 82% of carbon from the methane oxidation process formed carbon monoxide, methane values in Antarctica and Tasmania would be about 4 ppb less the current simulation predicts, eliminating the model overestimations, but also leading to slight underestimations in early spring. An alternate hy-

pothesis is that the slightly high bias indicates too much biogenic hydrocarbon oxidation in the Southern Hemisphere. Model-measurement differences peak during times when the contribution of CO from biogenic sources is largest, shown as the blue line in Plate 1h (e.g., July at Cape Grim, August and September at Syowa and the South Pole). Vertical profiles from aircraft data and the model (R13 and R14, Table 3) indicate that carbon monoxide concentrations decrease with height above 350 mbar, also observed in regions R19 and R25 in the Arctic (Figure 10).

6. Sensitivity Analysis

In an effort to understand the overall sensitivity of the CO chemistry-transport system, as well as diagnose model shortcomings, model runs have been conducted with varied source and sink fields, with the resulting CO distribution compared to the base case discussed above. The sensitivity of the monthly mean CO distribution to each individual source is proportional to the fractional contribution of that source to the CO distribution. Thus a 30% change in the fossil fuel changes the total CO concentration by 15% when fossil fuel contributes 50% to the CO budget, whereas the CO concentration is only changed by 3% when fossil fuel contributes, say, 10% to the CO budget. This straightforward relationship permits us to estimate how errors in the CO source terms may show up in the simulated CO fields. Before discussing uncertainty in each source term individually, we first consider the sensitivity of the simulated CO to the prescribed hydroxyl fields.

To investigate the model response to the OH fields, simulations were run with the base case (15% increase over *Spivakovsky et al.* [1990]) OH field, as well as with a low-OH case [*Spivakovsky et al.*, 1990] (unmodified), and a high-OH case [30% increase over *Spivakovsky et al.*, 1990]. As discussed, CO is assumed to have four sources and one sink, plus advection which acts locally as either a sink or a source. Of the four sources, only methane oxidation depends on hydroxyl concentration, increasing with larger OH values. We may calculate a maximum theoretical decrease in CO due to a 30% increase in OH by stepping into a box model framework. If we imagine an air parcel at the ground, the change in CO concentration over time depends on CO sources (emissions into the box and advection of CO into the box from adjacent parcels) and CO sinks (destruction by the OH radical and advection of CO out of the box). Changes in OH would have the largest effect on CO when it acts as the only sink (i.e., when no negative advection, or advection out of the box, occurs) and when no sources depend positively on OH to offset its role in CO destruction. Under this no-negative-advection, no-OH-dependent-sources case, the change in CO would be inversely proportional to the increase in OH, yielding a decrease in CO of 23%. In practice, this condition is approached when the contribution from methane oxidation is small and when there is no local sink due to advection. Figures 11a-11d show CO response to the 30% change in hydroxyl concentrations. In general, at higher altitudes and over the oceans, the model sensitivity approaches the 23% limit with large areas of the globe showing 15-20% decreases from the base case CO concentration. This observation agrees with our box model thinking: away from major emissions sources, advection acts more as a local source than as a local sink, so we would expect the OH sensitivity to be higher in these regions. In contrast, near source regions at the surface, the sensitivity drops quickly, with CO changing as little as 4% over regions with strong biomass burning.

From this spatial pattern of CO response we see that the local carbon monoxide concentrations near polluted areas do not depend strongly on local chemistry, but are determined instead by emissions and transport. Thus model errors near source regions cannot be well-explained by problems in the specified OH and must be attributed to incorrect source estimation or improper transport.

We have compared the three scenarios of hydroxyl fields with ground-based and aircraft measurements and consider the number of seasonally averaged data points which fall within 25% error bounds to be a reasonable diagnostic of model performance (Figure 7). In the base case run, 93% of the points fall in this range. In the low-OH scenario this agreement is 91%, and in the high-OH scenario it drops to 85%. Using the same type of analysis on the aircraft data (Figure 9), we find that 79% of the data points fall within the 25% error bounds in the base case run, versus 72% for low-OH case and 76% for high-OH case. CO from the low-OH run shows a distinct high bias, and CO from the high-OH run shows a distinct low bias.

We now return to the question of uncertainty in the CO distribution due to uncertainties in the individual source terms. As evidenced in Table 1, our annual fossil fuel emissions of 300 Tg/yr is the lowest of recent studies. As sensitivity is proportional to the fractional contribution of fossil fuel (see Figures 4a-4d), the greatest potential impact of errors in the fossil fuel source would be seen through the Northern Hemisphere, and specifically in the neighborhood of strong emissions, such as over the northeastern United States, Europe, and East Asia. Through our comparison of model results with observations, we have identified regions where errors in the fossil fuel source could explain differences. It has been noted that for a number of regions dominated in the springtime by fossil fuel CO, the model underestimates concentrations relative to observed values. This behavior is seen in varying degrees at most Arctic sites, most western U.S. sites, Mongolia, Midway Island, and Switzerland. Although the underestimate is most severe in the Arctic, we argue that fossil fuel alone cannot explain the high northern latitude low springtime values. Rather, we fault overly strong downward transport in the model's Arctic region, corroborated by evidence from GCTM ozone simulations, discussed earlier. To illustrate this point, we examine Barrow, Alaska, where the underestimation is particularly severe, and consider what increase in fossil fuel CO emissions would be needed to eliminate the difference with observed springtime values. In March at Barrow the model predicts CO values of 141 ppb (64 ppb of which is from fossil fuel CO). Observed values for March range from 187 ppb to 223 ppb. For fossil fuel alone to bring the total simulated March CO up to even the lowest observed March value (187 ppb), the CO from fossil fuel would have to increase from 64 ppb to 110 ppb, a 72% increase in the fossil fuel emission source, or 516 Tg (from our current 300 Tg estimate). This would clearly vault us to the far upper end of recent fossil fuel inventories (Table 1) and would produce an overestimation in regions of good agreement or less severe underestimation. While a less drastic increase in fossil fuel emissions could improve overall agreement, it must be noted that some regions, particularly in Europe, would suffer from such an increase. For instance, model CO values in Hungary during the summer are already higher than those observed, most likely due to too

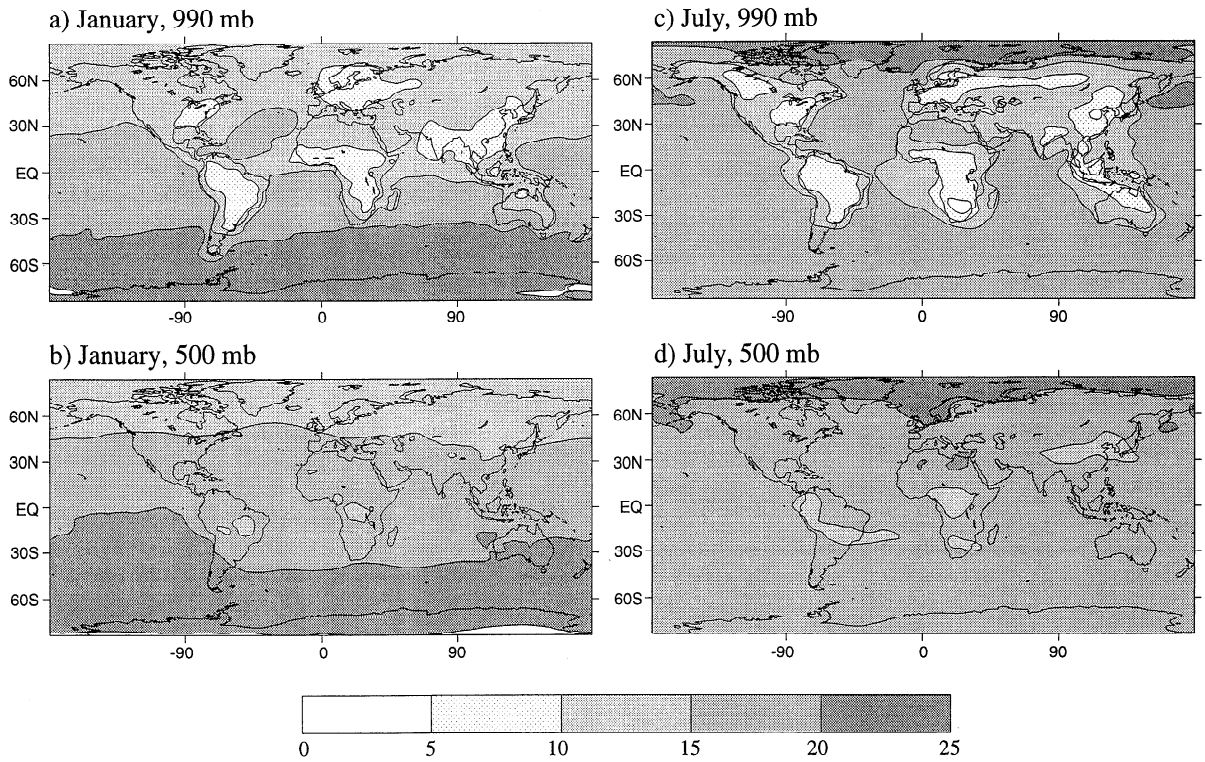

Figure 11. Percentage decrease in CO due to a 30% increase in OH. (a) January, 990 mbar. (b) January, 500 mbar. (c) July, 990 mbar. (d) July, 500 mbar.

much fossil fuel emissions in this region or improper transport.

Uncertainty in the biomass burning source may arise from either the magnitude or seasonality of the emissions. Our estimate of biomass burning falls on the high end (at 748 Tg CO/yr) of the 370-800 Tg CO/yr range of estimates in other studies (Table 1). However, there is no clear indication that this global total is unrealistically high. There are, however, three specific areas which may have unrealistically strong emissions, as indicated by the comparison with observations. These regions include the Amazon (where model results are much higher than low-level CO from aircraft data in the spring and summer), northern Africa (where biomass burning emissions contribute to an unobserved peak in November CO at Barbados), and the Korean Peninsula which exhibits a clear plume of CO from biomass burning not observed. While this Korean plume is due in large part to atypical transport (discussed previously), improper emissions may well contribute to error. Just as transport obscures the diagnosis of problems with biomass burning in Asia, similarly biogenic hydrocarbon oxidation likely contributes to the model-observation discrepancies over South America.

Like biomass burning, our estimate of CO produced from the oxidation of biogenic hydrocarbons in the model is higher than most other estimates of recent studies (Table 1). In our conversion of the hydrocarbon emissions to CO emissions, additional uncertainty was introduced by way of using a "high-NO_x" yield rate uniformly, rather than a yield dependent on local values of NO_x. It is worth noting, however, that uncertainties in the OH field do not effect the biogenic hydrocarbon oxidation estimates, as no oxidation calculations are performed in the model. Rather, it is assumed that the hydrocarbons are immediately oxidized thus entering the model as surface emissions of CO. In addition to the potential overestimation of CO in the Amazon, our comparison with data revealed too much biogenic hydrocarbon CO in the southeastern United States and possibly throughout the Southern Hemisphere, as indicated by the summer/fall CO overestimation in low southern latitudes. However, the influence of biogenic hydrocarbon oxidation on CO at Antarctica and Tasmania is difficult to assess reliably since CO from methane oxidation contributes the largest fraction to these sites.

Our estimate of the CO from methane oxidation may be too high due to the 100% oxidation yield assumed in the model. Other sources of potential uncertainty, however, are rather well-constrained. Owing to its long lifetime, CH_4 is well mixed throughout each hemisphere, with hemispheric values well-known. Although the CO produced by methane oxidation depends on the OH fields (which, as discussed, are the subject of some uncertainty), these same OH fields are responsible for the destruction of the CO they produce, so the uncertainties from OH cancel out when considering methane oxidation. In the low southern latitudes, too much methane oxidation could explain the model overestimation.

As noted in our earlier discussion of CO sources and sinks in the model, we have omitted CO released directly from the ocean, CO produced by the oxidation of anthropogenic nonmethane hydrocarbons (NMHCs), CO released directly from plants, and the soil sink for CO. The effect of our neglecting these budget terms is difficult to ascertain from the present analysis. As noted in Table 1, the ocean source for CO is small by all accounts (estimates range from 0-50 Tg CO/yr),

so we would not expect our results to change much even if this source were included. If we had included NMHCs from fossil fuel or biomass burning, the effect of these compounds would be to increase the magnitude of these two existing CO sources in the model. However, the effects of modifying the sources to include NMHCs would be difficult to distinguish from a straightforward change in the direct CO emissions, given the current uncertainty associated with both sources. Similarly, the effect of direct emissions from plants could be estimated by slightly increasing our biogenic hydrocarbon oxidation source. Finally, including a soil sink for CO would increase the loss rate of CO over land. However, as noted, our OH fields may already be too high over land, thus compensating for possible errors introduced by the neglect of this land sink.

The identified regions and seasons of possible errors in our emission fields admittedly may be incomplete. Additional measurement data (e.g., ground-based time series data in the Amazon) could aid in identifying and constraining model uncertainties. In light of available data, however, the relatively close agreement of our model results suggests that overall the CO emission sources employed for this study are reasonable estimates of the actual emissions of CO from fossil fuel burning, biomass burning, biogenic hydrocarbon oxidation, and methane oxidation. While it is possible that gross errors in one source are compensated by some combination of gross errors in other sources, model transport, and hydroxyl concentrations, this explanation seems to be an unlikely explanation for the generally realistic global simulation. Rather, we feel it most valuable to assume that model-observation agreement acts as a likely indicator of a realistic global CO simulation, and focus on areas of model-observation disagreement to gain insight into uncertainties in the emission sources.

7. Conclusions

The numerical simulation of carbon monoxide distribution presented here provides an opportunity to examine global patterns of CO distribution and dissect the contributing sources in order to gain a more complete understanding of controlling factors. By comparing model results with observations from the NOAA/CMDL global cooperative flask sampling network, with EMPA data from the Jungfraujoch station, and with aircraft data from the NASA Global Troposphere Experiment missions, we find that the CO concentrations simulated by the GFDL GCTM agree well with observations at most sites. Since our model results exhibit good agreement with observations, we may use it as a tool to explore the spatial and seasonal variability in the carbon monoxide budget.

We began our analysis with the following assumptions on emissions of CO into the atmosphere: fossil fuel burning contributes 300 Tg CO /yr; biomass burning contributes 748 Tg CO/yr; biogenic hydrocarbon oxidation contributes 683 Tg CO/yr; and methane oxidation contributes 760 Tg CO/yr. The assumed single sink for CO in our model is destruction by the hydroxyl radical, which we uniformly scale to agree with a methyl chloroform lifetime of 4.8 years (a 15% increase in the *Spivakovsky et al.* [1990] estimates). This hydroxyl field produces a CO lifetime varying from 10 days over summer continental regions to well over a year at the winter poles, shown in Figures 2a-2d.

Although this hydroxyl field is an important determinant of the global carbon monoxide distribution, the importance of this chemical sink relative to transport varies spatially. The response of CO to changes in the hydroxyl concentration varies greatly between strong source regions, where a 30% increase in OH results in CO decreases as small as 4%, and distant polar air, where the sensitivity is over 20%.

In order to diagnose the accuracy of emission inputs and hydroxyl fields, we analyze the controlling mechanisms of the model's simulated carbon monoxide distribution. The comparison of model-generated and observed time series data (from NOAA/CMDL and EMPA) indicates frequent underestimation of CO concentrations during the spring in areas where fossil fuel dominates the CO budget (especially the Arctic and western North America). While some of the most severe underestimations also arise from transport problems, we judge that overall our employed fossil fuel emission field is too low. Although CO results suggest certain areas of questionable biomass burning timing and magnitude, in most regions where biomass burning plays the dominant role, agreement between model and measurements is generally good. Problems with the oxidation of biogenic hydrocarbons are more difficult to isolate from the available data. One outstanding erroneous region is Grifton, North Carolina, where a large summertime biogenic CO peak occurs in the model and not in observations. In addition, biogenic emissions in the Southern Hemisphere may be too high, resulting in model overestimation of CO in the low southern latitudes in the late summer. Methane oxidation may also be too high, offering a competing explanation to the overestimation in the model of these summer low southern latitude sites.

Although the local seasonality of carbon monoxide is often controlled by the emissions, transport, and chemical destruction of a single source, such as fossil fuel through much of the Northern Hemisphere and biomass burning in the tropics, all sources are important in determining the magnitude of CO concentrations throughout the troposphere. CO from biomass burning and biogenic hydrocarbon oxidation each contribute over 15% to the total CO concentration everywhere. CO from methane oxidation does not exhibit strong spatial or seasonal variability and contributes about 25 ppb throughout the lower troposphere. Fossil fuel is the only source for CO which shows a clear hemispheric gradient, with large regions of >45% fossil fuel contribution in January at the surface, then dropping to less 10% in the low southern latitudes.

While our work in breaking down the seasonally varying components of the CO budget aids in diagnosing source uncertainties, it also contributes in estimating the breakdown of the CO budget at a number of observation sites. We would be interested in seeing how model results such as these compare with CO isotope measurements aimed at quantifying anthropogenic and natural contributions to the CO budget. With carbon monoxide, as other issues in atmospheric chemistry, the greatest potential for understanding lies in combining the research strengths of field measurements, laboratory studies, and numeric modeling.

Acknowledgments. We wish to thank Meredith Galanter for developing the updated biomass burning source, and James Yienger for developing the updated fossil fuel combustion source. The comments of David Baker, William Cooke, Meredith Galanter, and Dale Allen have all been very helpful in improving the paper, as were the suggestions made by anonymous reviewers. We thank Christoph Zellweger and EMPA for providing measurement data from Jungfraujoch, Switzerland, as well as the Carbon Cycle Group of NOAA/CMDL and the NASA Global Tropospheric

Experiment for their extensive data sets. T.A.H. wishes to thank support from an NSDEG Fellowship, and from NASA grant NGT530137. P.S.K. was supported by the Atmospheric Chemistry Project of the NOAA Climate and Global Change Program under grant NA36GP0250, and by the National Science Foundation under grant ATM-9213643.

References

Allen, D. J., P. Kasibhatla, A. M. Thompson, R. B. Rood, B. G. Doddridge, K. E. Pickering, R. D. Hudson, and S.-J. Lin, Transport-induced interannual variability of carbon monoxide determined using a chemistry and transport model, *J. Geophys. Res., 101,* 28,655-28,669, 1996.

Andreae, M. O., Biomass burning: Its history, use, and distribution and its impact on environmental quality and global climate, in *Global Biomass Burning: Atmospheric, Climatic, and Biospheric Implications,* edited by J. S. Levine, pp. 3-21, MIT Press, Cambridge, Mass., 1991.

Bakwin, P. S., P. P. Tans, and P. C. Novelli, Carbon monoxide budget in the Northern Hemisphere, *Geophys. Res. Lett., 21,* 433-436, 1994.

Baltensperger, U., H. W. Gaeggeler, J. T. Jost, M. Lugauer, M. Schwikowski, P. Seibert, and E. Weingartner, Aerosol climatology at the high-alpine sit Jungfraujoch, Switzerland, *J. Geophys. Res., 102,* 19,707-19,715, 1997.

Bates, T. S., K. C. Kelly, J. E. Johnson, and R. H. Gammon, Regional and seasonal variations in the flux of oceanic carbon monoxide to the atmosphere, *J. Geophys. Res., 100,* 23,093-23,101, 1995.

Benkovitz, C. M., M. T. Scholtz, J. Pacyna, L. Tarrason, J. Dignon, E. C. Voldner, P. A. Spiro, J. A. Logan, and T. E. Graedel, Global gridded inventories of anthropogenic emissions of sulfur and nitrogen, *J. Geophys. Res., 101,* 29,239-29,253, 1996.

Berntsen, T. K., and I. S. A. Isakson, A global three-dimensional chemical transport model for the troposphere, 1, Model description and CO and ozone results, *J. Geophys. Res., 102,* 21,239-21,280, 1997.

Blake, N. J., D. R. Blake, B. C. Sive, T.-Y. Chen, F. S. Rowland, J. E. Collins Jr., G. W. Sachse, and B. E. Anderson, Biomass burning emissions and vertical distribution of atmospheric methyl halides and other reduced carbon gases in the South Atlantic region, *J. Geophys. Res., 101,* 24,151-24,164, 1996.

Brasseur, G. P., D. A. Hauglustaine, S. Waters, P. J. Rasch, J.-F. Muller, C. Granier, and X. X. Tie, MOZART, a global chemical transport model for ozone and related chemical tracers, 1, Model description, *J. Geophys. Res., 103,* 28,265-28,289, 1998.

Chameides, W. L., P. S. Kasibhatla, J. J. Yienger, H. Levy II, and W. J. Moxim, The growth of continental-scale metro-agro-plexes, regional ozone pollution, and world food production, *Science, 264,* 74-77, 1994.

Chappellaz, J., T. Blunier, S. Kints, A. Dallenbach, J.-M. Barnola, J. Schwander, D. Raynaud, and B. Stauffer, Changes in the atmospheric CH_4 gradient between Greenland and Antarctica during the Holocene, *J. Geophys. Res., 102,* 15,987-15,997, 1997.

Crutzen, P. J., and M. O. Andreae, Biomass burning in the tropics: Impact on atmospheric chemistry and biogeochemical cycles, *Science, 250,* 1669-1678, 1990.

Dlugokencky, E. J., L. P. Steele, P. M. Lang, and K. A. Masarie, The growth rate and distribution of atmospheric methane, *J. Geophys. Res., 99,* 17,021-17,043, 1994.

Energy Information Administration (EIA), International energy outlook 1997, *Rep. DOE/EIA-0484(97),* Dept. of Energy, Washington, D. C., 1997.

Environmental Protection Agency (EPA), National air pollutant emission trends, 1900-1996, *Rep. EPA-454/R-97-011,* Research Triangle Park, N. C., 1997.

Fishman, J., J. M. Hoell Jr., R. J. Bendura, R. J. McNeal, and V. W. J. H. Kirchhoff, NASA GTE TRACE-A experiment (September-October 1992): Overview, *J. Geophys. Res., 101,* 23,865-23,880, 1996.

Fuelberg, H. E., R. E. Newell, S. Longmore, Young Zhu, D. J. Westberg, and E. V. Browell, A meteorological overview of the PEM-Tropics period. *J. Geophys. Res., 104,* 5585-5622, 1999.

Galanter, M. K., H. Levy II, and G. Carmichael, Impacts of biomass burning on tropospheric CO, NO_x, and O_3, *J. Geophys. Res.,* in press, 2000.

Guenther, et al., A global model of natural volatile organic compound emissions, *J. Geophys. Res., 100,* 8873-8892, 1995.

Hao, W. M., and M. H. Liu, Spatial and temporal distribution of tropical biomass burning, *Global Biogeochem. Cycles, 8,* 495-603, 1994.

Harriss, R. C., et al., Amazon Boundary Layer Experiment (ABLE 2A): Dry season 1985, *J. Geophys. Res., 93,* 1351-1360, 1988.

Harriss, R. C., et al., Amazon Boundary Layer Experiment: Wet season 1987, *J. Geophys. Res., 95,* 16,721-16,736, 1990.

Harriss, R. C., et al., Arctic Boundary Layer Expedition (ABLE 3A): July-August 1988, *J. Geophys. Res., 97,* 16,383-16,394, 1992.

Harriss, R. C., S. C. Wofsy, J. M. Hoell Jr., R. J. Bendura, J. W. Drewry, R. J. McNeal, D. Pierce, V. Rabine, and R. L. Snell, Arctic Boundary Layer Expedition (ABLE 3B), July-August 1990, *J. Geophys. Res., 99,* 1635-1644, 1994.

Hauglustaine, D. A., G. P. Brasseur, S. Waters, P. J. Rasch, J.-F. Muller, L. K. Emmons, and M. A. Carroll, MOZART, a global chemical transport model for ozone and related chemical tracers, 2, Model results and evaluation, *J. Geophys. Res., 103,* 28,291-28,335, 1998.

Hoell, J. M., Jr., D. L. Albritton, G. L. Gregory, R. J. McNeal, S. M. Beck, R. J. Bendura, and J. W. Drewry, Operational overview of NASA GTE/CITE 2 airborne instrument intercomparisons: Nitrogen dioxide, nitric acid, and peroxyacetyl nitrate, *J. Geophys. Res., 95,* 10,047-10,054, 1990.

Hoell, J. M., Jr., et al., Operational overview of the NASA GTE/CITE 3 airborne instrument intercomparisons for sulfur dioxide, hydrogen sulfide, carbonyl sulfide, dimethyl sulfide, and carbon disulfide, *J. Geophys. Res., 98,* 23,291-23,304, 1993.

Hoell, J. M., D. D. Davis, S. C. Liu, R. E. Newell, M. Shipham, H. Akimoto, R. J. McNeal, R. J. Bendura, and J. W. Drewry, Pacific Exploratory Mission West-A (PEM West-A): September-October 1991, *J. Geophys. Res., 101,* 1641-1653, 1996.

Hoell, J. M., D. D. Davis, S. C. Liu, R. E. Newell, H. Akimoto, R. J. McNeal, and R. J. Bendura, Pacific Exploratory Mission-West Phase B: February-March 1994, *J. Geophys. Res., 102,* 28,223-28,240, 1997.

Intergovernmental Panel on Climate Change (IPCC), *Climate Change 1992, The Supplementary Report to the IPCC Scientific Assessment,* Cambridge Univ. Press, New York, 1992.

Kanakidou et al., 3-D global simulations of tropospheric CO distributions - results of the GIM/IGAC intercomparison 1997 exercise, *Chemosphere: Global Change Science, 1,* 263-282, 1999.

Kasibhatla, P., H. Levy II, A. Klonecki, and W. L. Chameides, Three-dimensional view of the large-scale tropospheric ozone distribution over the North Atlantic Ocean during summer, *J. Geophys. Res., 101,* 29,305-29,316, 1996.

Kasibhatla, P., W. L. Chameides, and J. St. John, A three-dimensional global model investigation of seasonal variations in the atmospheric burden of anthropogenic sulfate aerosols, *J. Geophys. Res., 102,* 3737-3759, 1997.

Klonecki, A. A., Model study of the tropospheric chemistry of ozone, Ph.D. thesis, Princeton Univ., Princeton, N. J.,1999.

Klonecki, A., and H. Levy II, Tropospheric chemical ozone tendencies in the CO-CH4-NO_y-H_2O system: Their sensitivity to variations in environmental parameters and their application to a global chemistry transport model study, *J. Geophys. Res., 102,* 21,221-21,237, 1997.

Levy, H., II, W. J. Moxim, P. S. Kasibhatla, and J. A. Logan, The global impact of biomass burning on tropospheric reactive nitrogen, in *Global Biomass Burning: Atmospheric, Climatic, and Biospheric Implications,* edited by J.S. Levine, pp. 363-369, MIT Press, Cambridge, Mass., 1991.

Levy, H., II, P. S. Kasibhatla, W. J. Moxim, A. A. Klonecki, A. I. Hirsch, S. J. Oltmans, and W. L. Chameides, Global impact of human activity on tropospheric ozone, *Geophys. Res. Lett., 24,* 791-794, 1997.

Levy, H., II, W. J. Moxim, A. A. Klonecki, and P. S. Kasibhatla, Simulated tropospheric NO_x: Its evaluation, global distribution, and individual source contributions, *J. Geophys. Res., 104,* 26,279-26,306, 1999.

Mahlman, J. D., and W. J. Moxim, Tracer simulations using a global general circulation model: Results from a midlatitude instantaneous source experiment, *J. Atmos. Sci., 35,* 1340-1374, 1978.

Manabe, S., and J. L. Holloway Jr., The seasonal variation of the tropical circulation as simulated by a global model of the atmosphere, *J. Atmos. Sci., 31,* 43-83, 1974.

Manabe, S., D. G. Hahn, and J. L. Holloway Jr., Seasonal variation of the hydrologic cycle as simulated by a global model of the atmosphere, *J. Geophys. Res., 80,* 1617-1649, 1975.

McKee, D. J. (Ed.), *Tropospheric Ozone, Human Health and Agricultural Impacts,* Lewis, Boca Raton, Fla., 1993.

Miyoshi, A., S. Hatakeyama, and N. Washida, OH radical-initiated photooxidation of isoprene: An estimate of global CO production, *J. Geophys. Res., 99,* 18,779-18,787, 1994.

Muller, J.-F., and G. Brasseur, IMAGES: A three-dimensional chemical transport model of the global troposphere, *J. Geophys. Res., 100,* 16,445-16,490, 1995.

Novelli, P. C., L. P. Steele, and P. P. Tans, Mixing ratios of carbon monoxide in the troposphere, *J. Geophys. Res., 97,* 20,731-20,750, 1992.

Olivier, J. S. J., A. F. Bouwman, C. W. M. Van Der Maas, and J. J. M Berdowski, Emission Database for Global Atmospheric Research (EDGAR), *Environ. Monit. and Assess., 31,* 93-106, 1994.

Olson, J. R., B. A. Baum, D. R. Cahoon, and J. H. Crawford, Frequency and distribution of forest, savanna, and crop fires over tropical regions during PEM-Tropics A, *J. Geophys. Res., 104,* 5865-5876, 1999.

Pinto, J. P., Y. L. Yung, D. Rind, G. L. Russell, J. A. Lerner, J. E. Hansen, and S. Hameed, A general circulation model study of atmospheric carbon monoxide, *J. Geophys. Res., 88,* 3691-3702, 1983.

Prinn, R. G., R. F. Weiss, B. R. Miller, J. Huang, F. N. Alyea, D. M. Cunnold, P. J. Fraser, D. E. Hartley, and P. G. Simmonds, Atmospheric trends and lifetime of CH_3CCl_3 and global OH concentrations, *Science, 269,* 187-192, 1995.

Richardson, J. L., An investigation of large-scale tropical biomass burning and the impact of its emissions on atmospheric composition, Ph.D. thesis, Ga. Inst. of Technol., Atlanta, 1994.

Sachse, G. W., R. C. Harriss, J. Fishman, G. F. Hill, and D. R. Cahoon, Carbon monoxide over the Amazon Basin during the 1985 dry season, *J. Geophys. Res., 93,* 1422-1430, 1988.

Sanhueza, E., Y. Dong, D. Scharffe, J. M. Lobert, and P. J. Crutzen, Carbon monoxide uptake by temperate forest soils: The effects of leaves and humus layers, *Tellus, Ser. B, 50,* 51-58, 1998.

Saylor, R. D., and L. K. Peters, The global numerical simulation of the distribution of CO in the troposphere, in *Air Pollution Modeling and Its Application VIII,* edited by H. van Dop and D. G. Steyn, Plenum, New York, 1991.

Seinfeld, J. H., *Atmospheric Chemistry and Physics of Air Pollution,* John Wiley & Sons, Inc., New York, 1986

Spivakovsky, C. M., R. Yevich, J. A. Logan, S. C. Wofsy, M. B. McElroy, and M. J. Prather, Tropospheric OH in a three-dimensional chemical tracer model: An assessment based on observations of CH_3CCl_3, *J. Geophys. Res., 95,* 18,441-18,471, 1990.

Streets, D. G., and S. T. Waldhoff, Biofuel use in Asia and acidifying emissions, *Energy, 23,* 1029-1042, 1998.

Tie, X., J. C.-Y. Kao, and E. J. Mroz, Net yield of OH, CO, and O_3 from the oxidation of atmospheric methane, *Atmos. Environ., Part A, 26,* 125-136, 1992.

van Aardenne, J.A., G.R. Carmichael, H. Levy II, D. Streets, and L. Hordijk, Anthropogenic NO_x emissions in Asia in the period 1990-2020, *Atmos. Environ., 33,* 633-646, 1999.

Wang, Y., J. A. Logan, and D. J. Jacob, Global simulation of tropospheric O_3-NO_x-hydrocarbon chemistry, 2, Model evaluation and global ozone budget. *J. Geophys. Res., 103,* 10,727-10,755, 1998.

Warneck, P., *Chemistry of the Natural Atmosphere, Int. Geophys. Ser.,* vol. 41, Academic, San Diego, Calif., 1988.

Yienger, J., A. A. Klonecki, H. Levy II, W. J. Moxim, and G. R. Carmichael, An evaluation of chemistry's role in the winter-spring ozone maximum found in the northern midlatitude free troposphere, *J. Geophys. Res., 104,* 3655-3667, 1999.

Zellweger, C., M. Ammann, B. Buchmann, P. Hofer, M. Lugauer, R. Ruettimann, N. Streit, E. Weingartner, and U. Baltensperger, Summertime NO_y speciation at the Jungfraujoch, 3580 m asl, Switzerland, *J. Geophys. Res.*, in press, 2000.

T. Holloway, Atmospheric and Oceanic Sciences Program, Princeton University, Princeton, NJ 08542. (tah@gfdl.gov)

P. Kasibhatla, Nicholas School of the Environment, Duke University, Durham, NC 27708.

H. Levy II, Geophysical Fluid Dynamics Laboratory, Princeton, NJ 08542-0308. (hl@gfdl.gov)

(Received May 4, 1999; revised December 1, 1999;
accepted December 7, 1999.)